

INDICE

Investigating the Accelerated Electrochemical Corrosion Protection Performance of Coal-Tar and Bitumen Enamel Coating for Pipelines.....2

A short review on various applications of carbon nanotubes and graphene nanosheets in different industries.....5

Evaluation and optimization of supercritical extraction of insulin from *Otostegia persica* 13

Effects of chemical and mechanical functionalization of carbon nanotubes on the behavior of a CNT/Phenolic nanocomposite.....20

The Wear Behavior of Au-Co/Diamond-Like Carbon Composite Electrochemical Coating.....26

Editorial

The carbon-based materials have been interested by researchers during the last decades because the carbon sources are abundantly available in the world wide. Today, these materials, in various forms including diamond, carbon black, pyrolytic carbon, glassy carbon, graphite, graphene, carbon nanotubes, carbon fibers, porous carbons and ..., play a principal role in different technology areas. The energy storage, coating, catalysis, medicine, pollutant absorber, electronic devices are some relevant applications of carbon -based materials.

In Iran, many research groups are working on the carbon structures with different applications to develop more sustainable and smart variants of them. In this issue, we are going to open a window in front of readers to have

better understand about the recent researchers efforts in Iran by presenting four papers on corrosion protection by carbon based coating, wear properties of diamond like carbon composite, CO₂ supercritical extraction and mechanical behavior of functionalized carbon nanotubes on the nanocomposite. Because of the introduction of new nano carbon structures has forced further the potential of carbon to nanotechnology applications in Iranian research groups, a brief review on the applications of carbon nanotubes and graphene nanosheets is another part of this issue.

Dr. Behzad Aghabarari
Tehran, February 2019

Editor Jefe:

M. Olga Guerrero Pérez
Universidad de Málaga

Editores:

Carolina Belver Coldeira
Universidad Autónoma de Madrid

Raúl Berenguer Betrián
Universidad de Alicante

Tomás García Martínez
Instituto de Carboquímica (CSIC)

Manuel J. Pérez Mendoza
Universidad de Granada

Fabián Suárez García
Instituto Nacional del Carbón
(CSIC)

Investigating the Accelerated Electrochemical Corrosion Protection Performance of Coal-Tar and Bitumen Enamel Coating for Pipelines

B. Aghabarari¹, S. Pourhashem², B. Moeinifard³

¹ Nanotechnology and Advanced Materials Department, Materials and Energy Research Center, Karaj, Iran

² Nanotechnology Research Center, Research Institute of Petroleum Industry (RIPI), Tehran, Iran

³ Department of Chemistry, Isfahan University of Technology, Isfahan, Iran

Corresponding author e-mail: b.aghabarari@merc.ac.ir

Abstract

This work attempts to give a general zoom to the nanostructured carbon materials from their appearance, discovery and fabrication, until their applications and impacts in the scientific field. The three main carbon nano-allotropes: fullerenes, carbon nanotubes and graphene, are revised in order to establish a general overview. Finally, some alternatives on the potential growing of these materials are also presented.

Keywords: Coal-Tar Enamel, Bitumen Enamel, Organic Coatings, Electrochemical Corrosion Tests

1. Introduction:

Corrosion of pipelines is an extreme challenge for oil and gas industry. The harsh environment of pipelines application has great effect on selecting the appropriate coatings for them. Different types of coatings are used for corrosion protection of pipelines in industry and meanwhile, coal-tar and bitumen enamel coatings are widely applied for enhancing their service-life [1-3].

Coal tar coating is blend of epoxy resins and coal tar with black color which is extremely used in harsh corrosive environments. Coal tar acts as filler in polymer matrix, providing high moisture resistance, UV resistance, thermal stability, toughness, and good adhesion to metallic substrate. These coatings show excellent resistance against salt water and cathodic disbondment and therefore, they are widely used for protection of off-shore metallic structures, ships submerged hull areas, cooling towers, and ballast tanks [1, 4, and 5].

Bitumen coatings are mainly composed of aliphatic hydrocarbons with good resistance against water and chemicals. They are extensively used as an alternative for coal tar coatings due to lower amounts of carcinogen in bitumen enamel coatings. However, these coatings have shortcomings regarding fume extraction during used and low flexibility at very low temperatures [1, 4].

Therefore, in this research, we have investigated the corrosion protection efficiency of industrially used coal-tar and bitumen coatings for pipe-lines.

2. Experimental:

Industrially used coal-tar and bitumen enamel coatings on mild steel substrates with dimension of 3 × 4 cm² are used for corrosion protection evaluations. The degradation process of coatings is examined in the

synthetic groundwater by electrochemical methods using Potentiostat/Galvanostat (PGSTAT 30). The electrochemical cell consists of the sample, Pt wire, and saturated calomel electrode (SCE) as working, counter, and reference electrode, respectively. The synthetic ground water with pH value of about 7.25 is used as corrosive electrolyte and its chemical composition is presented in Table 1.

Precursor	Amount (mg/mL)
CaCl ₂	133.2
MgSO ₄ ·7H ₂ O	59
NaHCO ₃	208
H ₂ SO ₄	85
HNO ₃	22.2

Table 1. Chemical composition of synthetic ground water.

The potentiodynamic polarization tests are repeated 7 times for accelerating the degradation of coatings. For potentiodynamic polarization tests, open circuit potential (OCP) of system at equilibrium state after immersion is recorded as corrosion potential (E_{corr}). Then, the polarization curve was plotted by sweeping the applied potential from -0.4 to +0.4 V with respect to OCP at scan rate of 1 mV/sec on 1 cm² anode. Corrosion current density (i_{corr}) was determined from Tafel plot by extrapolating the linear portion of the curve to E_{corr} . Tafel constants including anodic (β_a) and cathodic (β_c) slopes were calculated for anodic and cathodic parts of Tafel plot, respectively. The polarization resistance (R_p), corrosion rate (C.R.), the coating porosity (P), and the corrosion protection efficiency (PE) are calculated based on following equations [3, 6]:

$$R_p = \frac{\beta_a \beta_c}{2.303 (\beta_a + \beta_c) i_{corr}} \quad (1)$$

$$CR (mm/year) = \frac{3270 i_{corr} (A/cm^2) \cdot EW}{D (\beta/cm^2)} \quad (2)$$

$$P = \frac{R_p^{substrate}}{R_p^{coat}} \times 10^{-|\Delta E_{corr}/\beta_a^{substrate}|} \quad (3)$$

$$PE\% = 100 \times \left(1 - \frac{R_p^{substrate}}{R_p^{coat}}\right) \quad (4)$$

Then, the corrosion protection performance of coatings is determined by electrochemical impedance

spectroscopy (EIS). The EIS tests were carried out in frequency range of 10^{-2} to 10^5 Hz with AC amplitude of 10 mV at OCP. All electrochemical tests are repeated three times.

3. Results and discussion:

Fig. 1 shows the OCP values of samples during immersion in synthetic groundwater. Accordingly, the coated substrates have more positive OCP values compared to bare one. Meanwhile, the type of coating has great effect on OCP values of samples; the OCP value of the coal-tar enamel coated sample is more noble than bitumen enamel sample.

Fig. 2 shows the potentiodynamic polarization curves of samples. The results derived from polarization curves are presented in Table 2. The results derived from potentiodynamic polarization tests show that coal-tar coated sample has more positive E_{corr} , lower i_{corr} , lower porosity, higher polarization resistance (R_p) and higher corrosion protection efficiency (PE); revealing enhanced corrosion protection capability

of coal-tar enamel coating compared to bitumen enamel coated sample. Indeed, the corrosion rate for bare substrate, bitumen enamel coating, and coal-tar enamel coating is 0.07502, 0.00904, and 0.00159 mm/year, respectively. The calculated coating porosity for bitumen enamel coating and coal-tar enamel coating is 1.81% and 0.05%, respectively; therefore, the higher corrosion resistance of coal-tar epoxy coatings can be attributed to the lower amount of porosity and defects in its structure, compared to bitumen enamel coating.

Moreover, the EIS results including Bode and Nyquist plots are presented in Fig. 3 and Fig. 4, respectively. The Bode plots indicate that the Z modulus for coatings at low frequency of 0.01 Hz ($|Z|_{0.01\text{Hz}}$) is significantly more than bare sample. The $|Z|_{0.01\text{Hz}}$ value for coal-tar enamel sample and bitumen enamel sample is 24.5×10^4 and 5.1×10^4 Ohm.cm², respectively. The higher Z modulus of coal-tar sample confirms that the coal-tar enamel coating is more appropriate for achieving enhanced corrosion protection for pipelines due to their higher corrosion resistance.

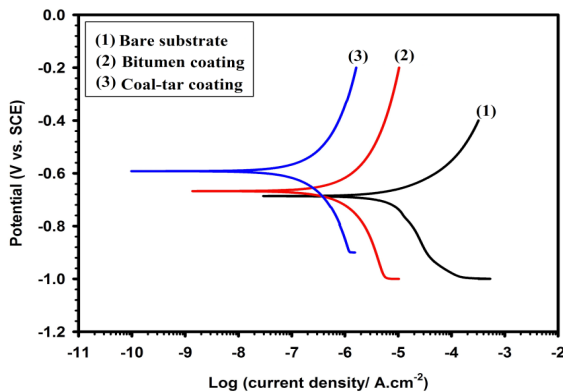


Figure 1. The variation of OCP for bare substrate, bitumen enamel and coal-tar enamel coating.

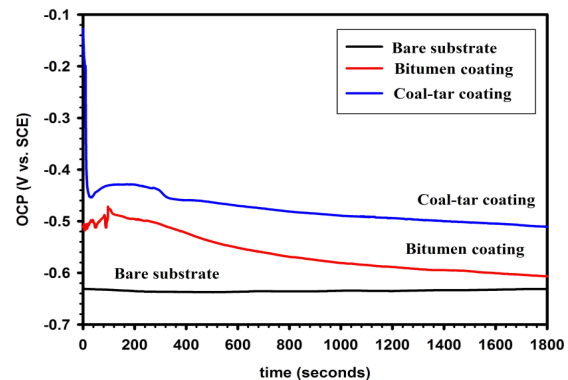


Figure 2. The potentiodynamic polarization curves for bare substrate, bitumen enamel and coal-tar coating.

Sample	E_{corr} (V/SCE)	i_{corr} ($\mu\text{A}/\text{cm}^2$)	β_a (V/dec)	β_c (V/dec)	C.R. (mm/year)	R_p ($\text{k}\Omega.\text{cm}^2$)	PE (%)	P (%)
Bare substrate	-0.691	6.4	0.102	0.237	0.07502	4.81	-	-
Bitumen coating	-0.675	0.778	0.264	0.260	0.00904	73.16	95.42	1.81
Coal-tar coating	-0.599	0.136	0.256	0.171	0.00159	326.18	98.98	0.05

Table 2. The electrochemical parameters derived from polarization curves.

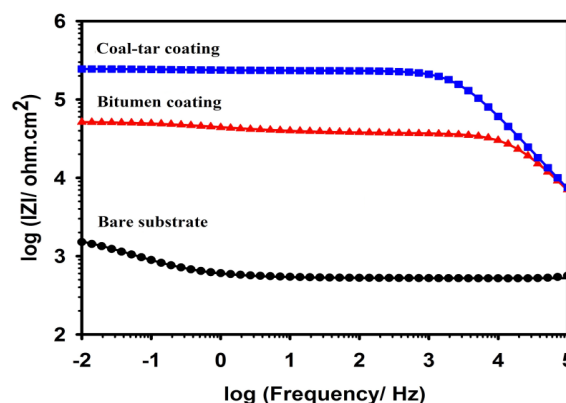


Figure 3. The Bode plots for bare substrate, bitumen enamel and coal-tar enamel coating.

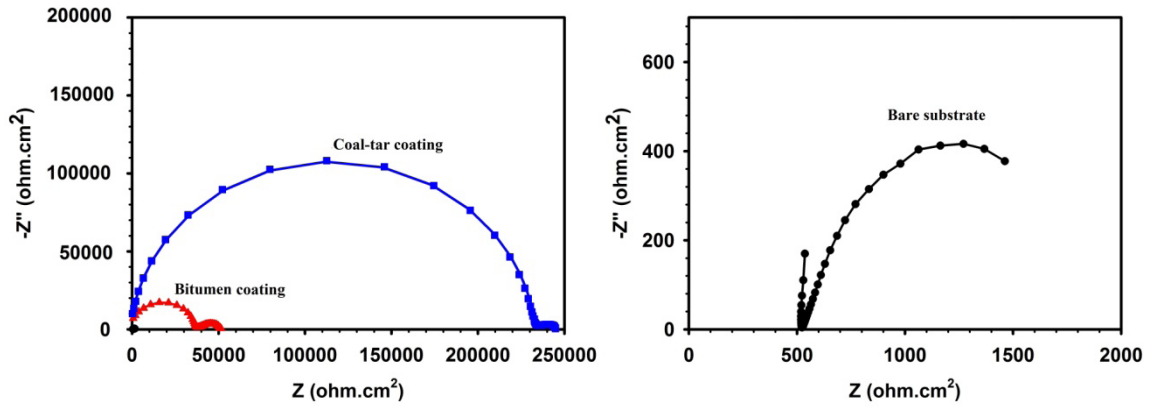


Figure 4. The Nyquist plots for bare substrate, bitumen enamel and coal-tar enamel coating.

Further, the results of EIS are fitted by electrical equivalent circuit (Fig. 5) by using NOVA software. The proposed equivalent circuit consists of solution resistance (R_s), coating constant phase element (Q_{coat}), pore resistance (R_{pore}), double layer constant phase element (Q_{dl}), and charge transfer resistance (R_{CT}). The calculated parameters are mentioned in Table 3. The results show that the coating resistance and charge transfer resistance for coal-tar enamel coating is significantly more than bitumen enamel coating; revealing that the defects of coal-tar coatings are less than bitumen enamel coating. The enhanced

corrosion protection capability of this sample can be attributed to the pore structure and chemical composition of coal-tar enamel coating.

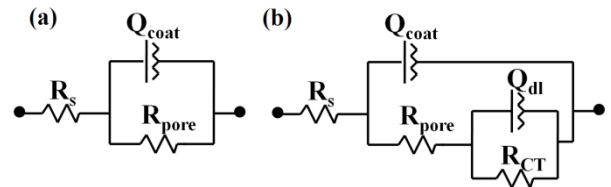


Figure 5. Electrical equivalent circuit used for fitting EIS results; (a) bare substrate, (b) coated substrate.

Sample	CPE _{coat}		R _{pore} (Ω cm ²)	CPE _{dl}		R _{ct} (Ω cm ²)
	Y ₀ (Ω ⁻¹ cm ⁻² s ⁿ)	n		Y ₀ (Ω ⁻¹ cm ⁻² s ⁿ)	n	
Bare substrate	-	-	-	2.52 × 10 ⁻³	0.634	1.3 × 10 ³
Bitumen coating	5.89 × 10 ⁻¹⁰	0.923	38.7 × 10 ³	2.79 × 10 ⁻⁵	0.528	15.5 × 10 ³
Coal-tar coating	4.40 × 10 ⁻¹⁰	0.947	234 × 10 ³	5.04 × 10 ⁻⁵	0.532	15.8 × 10 ³

Table 3. Calculated electrochemical parameters via electrical equivalent circuit.

Accordingly, coal-tar coatings have higher corrosion protection capability than bitumen enamel coatings. The improved corrosion resistance of coal-tar sample is due to lower amount of defects and pores in its structure. The compact structure of coal-tar can decrease the uptake of water and corrosive agents. Besides, coal-tar has is inherently hydrophobic and has higher adhesion strength to metallic substrate [5].

4. Conclusion:

In this research, the corrosion protection performance of coal-tar coating and bitumen enamel coating is investigated. The corrosion resistance of samples is considered by electrochemical methods. The results clearly indicate that coal-tar coated sample has higher corrosion protection efficiency than bitumen enamel coating.

Reference

[1] L. Niu, Y.F. Cheng, "Development of innovative coating technology for pipeline operation crossing the permafrost

terrain", *Const. Build. Mater.* 22 (2008) 417-422.

[2] S.M. Cambier, G.S. Frankel, "Coating and interface degradation of coated steel, Part 2: Accelerated laboratory tests", *Electrochim. Acta.* 136 (2014) 442-449.

[3] S.H. Lee, W.K. Oh, J.G. Kim, "Acceleration and quantitative evaluation of degradation for corrosion protective coatings on buried pipeline: Part II. Application to the evaluation of polyethylene and coal-tar enamel coatings", *Prog. Org. Coat.* 76 (2013) 784-789.

[4] S. Papavinasam, M. Attard, and R.W. Revie, "Evaluation of external pipeline coatings for corrosion protection-A review", *Corr. Rev.* 26 (2008) 373-438.

[5] S.D. Jagtap, S.P. Tambe, R.N. Choudhari, B.P. Mallik, "Mechanical and anticorrosive properties of nontoxic coal-tar epoxy alternative coating", *Prog. Org. Coat.* 77 (2014) 395-402.

[6] S.H. Lee, W.K. Oh, J.G. Kim, "Acceleration and quantitative evaluation of degradation for corrosion protective coatings on buried pipeline: Part I. Development of electrochemical test methods", *Prog. Org. Coat.* 76 (2013) 778-783.

A short review on various applications of carbon nanotubes and graphene nanosheets in different industries

B. Aghabarari¹, S. Pourhashem, M.R. Vaezi

¹ Nanotechnology and Advanced Materials Department, Materials and Energy Research Center, Karaj, Iran
Corresponding author e-mail: b.aghabarari@merc.ac.ir

Abstract

Carbon based nanomaterials including carbon nanotubes and graphene nanosheets have attracted the attention of researchers due to their outstanding extraordinary properties. In this article, we have presented the researches on the application of carbon nanotubes and graphene sheets in Nanotechnology and Advanced Materials at Materials and Energy Research Center. We have used different modification strategies based on its application for improving the obtained properties in various fields including ammonia gas sensors, supercapacitors, fuel cells, drug delivery systems, and corrosion resistant coatings in order to achieve superior properties in each field.

Keywords: Carbon nanostructures; Carbon nanotubes; Graphene; Surface modification.

1. Introduction

Carbon based nanomaterials including carbon nanotubes and graphene sheets have great potential for revolutionizing many aspects of our life [1]. The carbon nanotube as 1D and graphene as 2D allotropes of carbon nanostructures have unique properties in terms of electrical and thermal conductivity, mechanical performance and optical features [2]. They have been used in various fields due to their outstanding inherent properties. Therefore, in this article, we will introduce various applications of these nanomaterials by our research team in Department of Nanotechnology and Advanced Materials at Materials and Energy Research Center.

2. Carbon nanotubes

Carbon nanotube (CNT) is hexagonal network of carbon atoms rolled up into a seamless, hollow cylinder. CNT is one of the most investigated materials before invention of graphene. CNTs with intrinsic properties including high surface area, cylindrical structure, and high aspect ratio of length to diameter have attracted the attention of researchers. CNTs can be divided into two categories of single walled carbon nanotubes (SWCNTs) and multi-walled carbon nanotubes (MWCNTs). SWCNTs are made of a single graphene sheet wrapped around to form a cylinder and MWCNTs consist of two or more graphene sheets coaxially arranged around a central hollow core with van der Waals forces between adjacent layers [3]. Herein, we have presented different applications of CNTs discovered with our research team.

2.1. Ammonia gas sensors

Carbon nanotubes have great potential for

application in nano-electronic devices and semi-conducting SWCNTs can be a promising candidate for gas sensors due to significant electronic changes by gas adsorption. In this regard, F. Goudarzi et al. [4] considered the gas sensing properties of SWCNTs. They deposited SWCNTs doped with lithium on interdigitated electrode by using electrophoresis method and the deposited SWCNTs doped with lithium were heat treated at 350 °C for 5 h. The electrical response of the hybrid sensor was measured upon exposure to 500 ppm NH₃ at different operating temperatures between 25 °C to 280 °C. The electrical response and sensitivity of gas sensor are calculated based on equation 1 and 2, respectively:

$$\text{Sensor response} = I_g - I_0 \quad (1)$$

$$\text{Sensor selectivity} = [(I_g - I_0) / I_0] \times 100 \quad (2)$$

where I_0 and I_g are measured current of gas sensors upon exposure to air and ammonia, respectively. The variation of electrical response and sensitivity of gas sensor as a function of immersion time is shown in Figure 1. The results of Figure 1 (a) showed that the gas response increased by increasing the temperature and the sensor recovered rapidly by removing ammonia gas. Further, Figure 1 (b) indicated that the sensitivity of gas sensor increased with temperature due to improve of interaction between gas and sensor; however, the thermal desorption of ammonia molecules at higher temperatures, hindered the gas adsorption process and gas-sensor interaction. Therefore, the maximum gas response with high sensitivity of 34% was obtained at 150 °C [4].

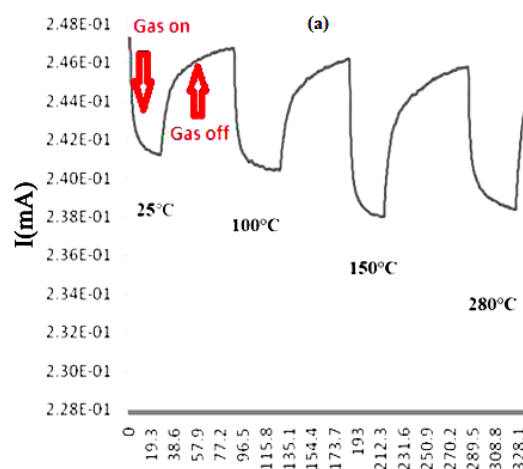


Figure 1. (a) response curves.

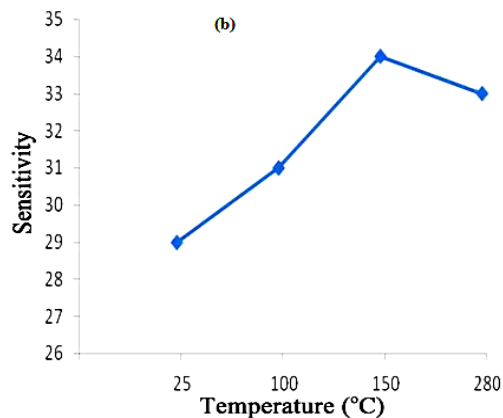


Figure 1. (b) sensor response of SWCNTs/Li sensor to 500 ppm NH_3 at 25, 100, 150 and 280°C [4].

2.2. Supercapacitors

Supercapacitors can be used in various fields including power source of camera flash, lasers, pulsed light generators, backup power source for computer memory. In this regard, Nikzad et al. [5] developed CNT/polyaniline nanocomposite via in situ polymerization of aniline. They considered the effect of pure CNT and $\text{HNO}_3/\text{H}_2\text{SO}_4$ acid treated CNT on electrochemical properties of the prepared supercapacitors. The cyclic voltametric curves indicated that acid treated CNT is much more electroactive than neat CNT; which can be assigned to developed functional groups on CNT. The results of galvanostatic curves in the applied current of 1 mA during 20 successive cycles are shown in Figure 2. Since the discharge time has straight relation with specific capacitance, the specific capacitance of nanocomposites is much bigger than pure acid treated CNT. The electrochemical results revealed

that the conductivity of the obtained nanocomposites increased and the supercapacitor behavior of polyaniline improves by adding CNT. Meanwhile, composites containing acid treated CNT showed higher conductivity compared to pure CNT [5].

3. Graphene

Graphene is the thinnest material with one-atom-thick which consists from sheets of sp^2 -bonded carbon atoms closely packed in a honeycomb crystal lattice. Graphene is the basic structure of graphite, carbon nanotubes and fullerene. Graphene shows unique properties such as high surface area (2630 m^2/g), high aspect ratio, low density, ultra-high mechanical strength Young modulus of ~ 1 TPa, tunable electronic band gap, high thermal conductivity (~ 5000 W/mK) and fast charge carrier mobility ($\sim 200,000$ $\text{cm}^2 \text{V}^{-1} \text{s}^{-1}$) [3, 6].

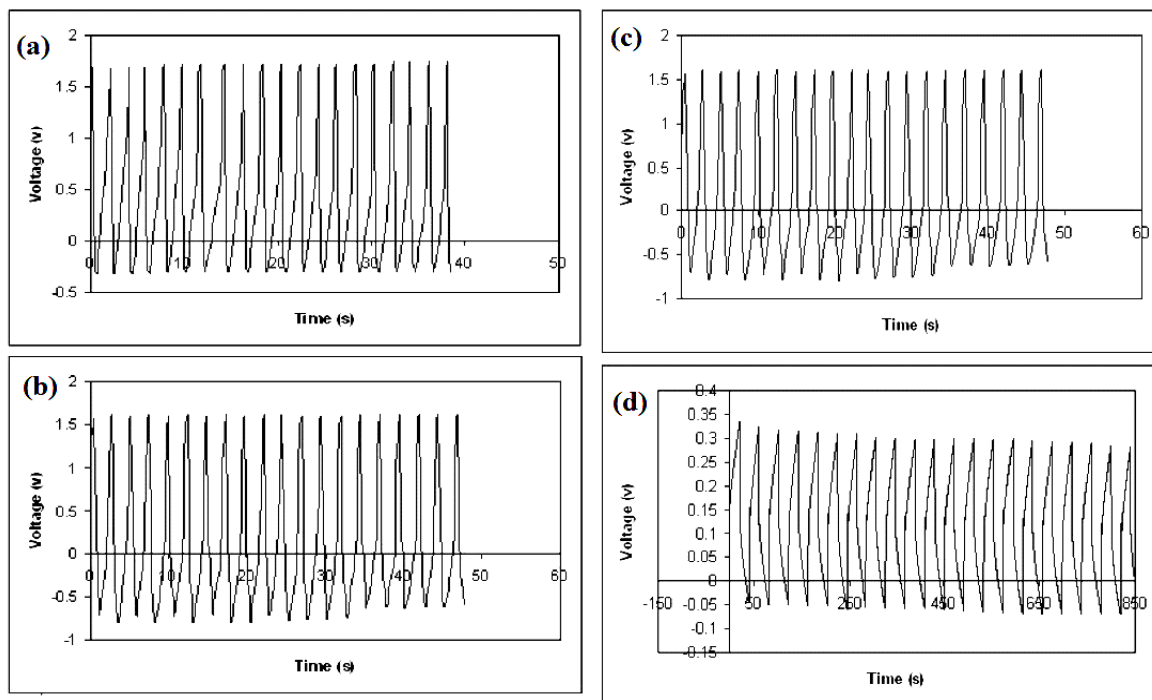


Figure 2. Galvanostatic curves of (a) CNT, (b) polyaniline/CNT composite, (c) acid treated CNT, and (d) polyaniline/acid treated CNT composite [5].

Our research team has used graphene and its derivatives such as graphene oxide (GO) for different

applications which are discussed below.

3.1. Drug delivery systems

Graphene and its derivatives show good biocompatibility and they can be applied in biomedical applications such as drug delivery, MRI, hyperthermia, bio-sensors and anti-bacterial materials.

Farazi et al. decorated the surface of graphene oxide with magnetic (Fe_3O_4) nanoparticles via co-precipitation method and then, they synthesized $\text{Fe}_3\text{O}_4/\text{GO}$ -gelatin nanocomposite to obtain a stable suspension. They used Fe_3O_4 nanoparticles due to their biocompatibility, low toxicity and acceptable magnetic properties. Also, gelatin was selected because it is a water-soluble biopolymer with advantages such as low-cost, non-toxicity and biodegradability. Further, they studied the potential application of the prepared nanocomposite as a

drug nano-carrier. Doxorubicin hydrochloride (DOX) is anti-breast cancer drug which could be loaded on the surface of different nano-carriers via π - π stacking for application in drug delivery systems. Therefore, Farazi et al. [7] loaded the DOX on the synthesized $\text{Fe}_3\text{O}_4/\text{GO}$ -gelatin nanocomposite and studied the effect of pH and temperature on releasing the drug. The results (Figure 3) showed that the amount of released DOX increased by increasing temperature from 25 °C to body temperature. The DOX cumulative release in 144 h was 8.84% and 20.98% at 25 °C and 37 °C, respectively. The DOX cumulative release increased from 20.98% to 41.98% by decreasing the pH from 7.4 to 5.4. Accordingly, the DOX drug is better released from the synthesized nanocomposite at body temperature and in acidic pH which mimics tumor environment [7].

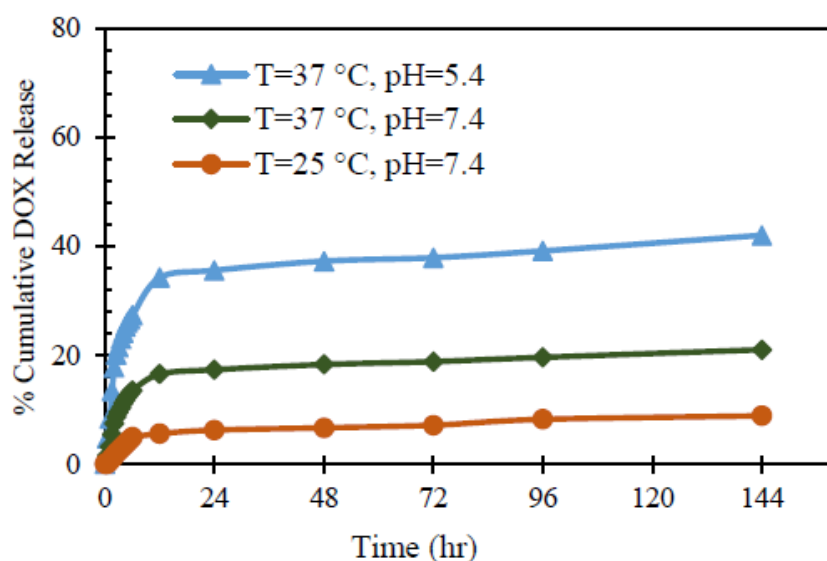


Figure 3. The in-vitro release profile of DOX from Fe₃O₄/GO-DOX [7].

3.1. Methanol oxidation in fuel cells

Proton exchange membrane fuel cells, with outstanding advantages such as low operation temperature and high voltage output, are an appropriate candidate for solving the world's energy power. Methanol oxidation is a promising alternative for next generation energy conversion systems. The main approach in direct methanol fuel cells is to oxidize methanol completely to carbon dioxide. However, commercialization of direct methanol fuel cell is challenging because of its low kinetics [8-10]. Various approaches have been considered for developing the reaction kinetics and to reduce the metal loading on the surface.

In this regard, Asghari et al. [11] prepared reduced graphene oxide and nitrogen doped graphene based platinum catalysts and compared the results with commercial Pt/C catalyst. Graphene with unique chemical and physical properties such as high specific surface area, ultra-thin thickness, electrical conductivity, structural flexibility and high stability can be used as support for fuel cell electrocatalysts. The XRD results for reduced graphene oxide (Pt/G) and nitrogen doped graphene (Pt/NG) based platinum catalysts are presented in Figure 4. According

to Figure 4, the characteristic peak of graphene oxide can be seen at $2\theta = 12^\circ$. In the case of G/Pt and NG/Pt, different facets of Platinum nanocrystals can be observed in XRD patterns beside the diffraction peaks at 27 to 29 degrees attributed to carbon support. The synthesized catalysts were evaluated for methanol and CO electro-oxidation. Figure 5 shows the cyclic voltammetry results of the synthesized catalysts. The results proved that the nitrogen doped graphene based platinum catalysts have higher electrochemical catalytic activity. Indeed, the Pt/NG catalysts showed higher comprehended peak current and higher ratio of forward peak to backward peak (I_f/I_b); announcing that Pt/NG sample is more stable toward intermediates of electro-oxidation of methanol (mostly CO) and therefore, higher stability can be achieved versus CO-poisoning of Pt nanoparticles. Moreover, although the onsets of three catalysts were almost the same, the Pt/G and Pt/NG showed faster pace to the forwarding peaks due to their higher current densities. The enhanced electrochemical performance of the synthesized catalyst is due to nitrogen functional groups on the surface of graphene sheets which can alter the defects and electronic structure of the support.

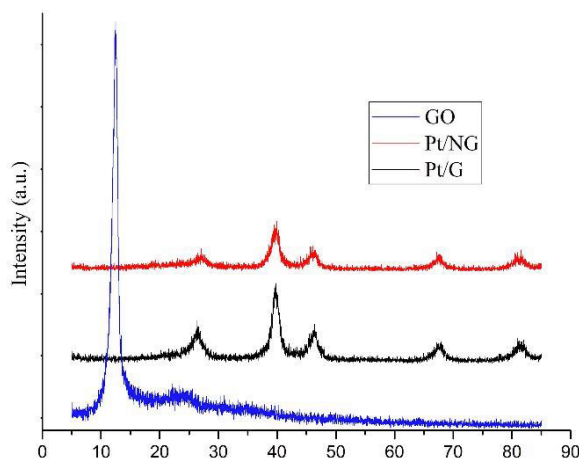


Figure 4. XRD patterns of GO, Pt/G and Pt/NG [12].

Moreover, Aghabarari et al. [12] synthesized N-doped graphene based Platinum nanocatalysts at different temperatures using melamine as nitrogen source and compared the results with commercial 40 wt.% platinum on carbon catalyst. As Figure 6 shows, proper distribution of nitrogen on the synthesized samples is observed by elemental mapping. Further, they characterized the electrochemically active surface area of catalysts by electrochemical methods. Figure 7 shows the CO stripping and the subsequent voltammograms in acidic media. The results present that the Pt/NG-400 and Commercial Pt/C catalysts behave approximately similar with each other in onset or peak potential. However, onset of Pt/NG-600 and Pt/NG-800 catalysts happens very faster than that of Pt/C (almost in 0.5 V in more negative potentials). In acidic media, all catalysts develop a main CO oxidation peak with some differences. For example, Pt/C presents only a symmetric peak at 0.61 V, while the other catalysts exhibit an asymmetrical peak with

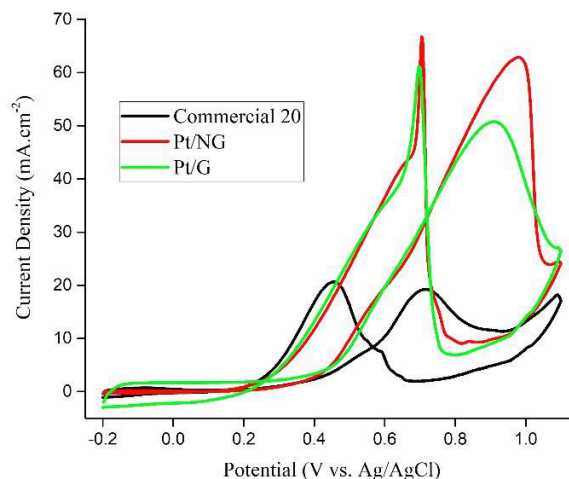


Figure 4. Methanol oxidation reaction in a three electrode half-cell measurements under Ar atmosphere at room temperature, 0.5 sulfuric acid and 2M methanol, normalized by CO-stripping surface area [11].

several humps. These small anodic contributions are linked to CO oxidation on catalytic sites of diverse nature. Catalytic sites of diverse activity justify the absence of only one symmetric main peak in conjunction with a CO diffusion impediment, which can be occasioned by adsorbed sulfate on special sites (e.g. edge) or by some geometric factor (e.g. particle agglomeration) that impedes the free CO diffusion towards the most catalytic sites. Additionally, an electronic charge transfer by the catalyst support may produce higher CO binding energy and consequently slower CO diffusion. Consequently, multiple anodic peaks associated with CO oxidation on different sites are observed during the CO stripping voltammogram [12]. Besides, methanol oxidation cyclic voltammetry results indicate that the synthesized N-doped graphene based catalysts have higher activity for methanol oxidation over commercial catalyst for fuel cell applications.

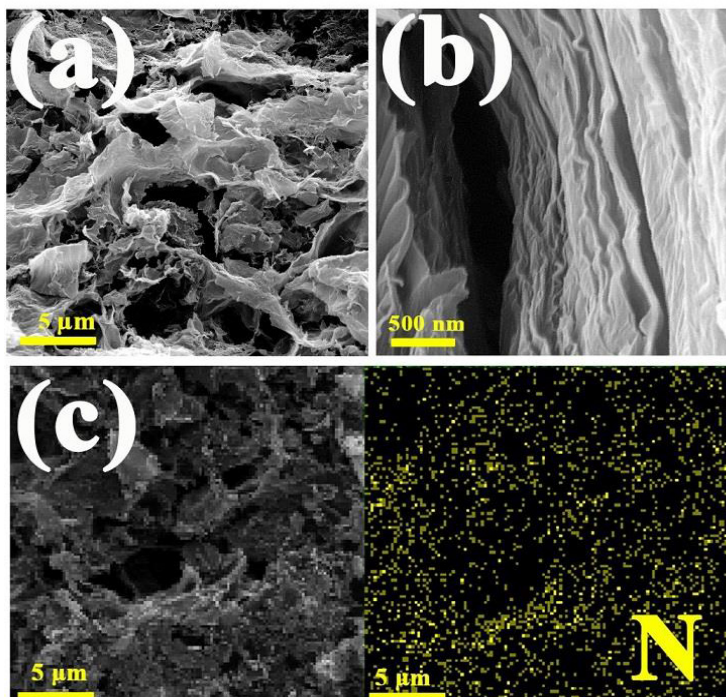


Figure 6. FE-SEM images of (a, b) GO and (c) NG sample synthesized at 800 °C with its nitrogen elemental mapping [12].

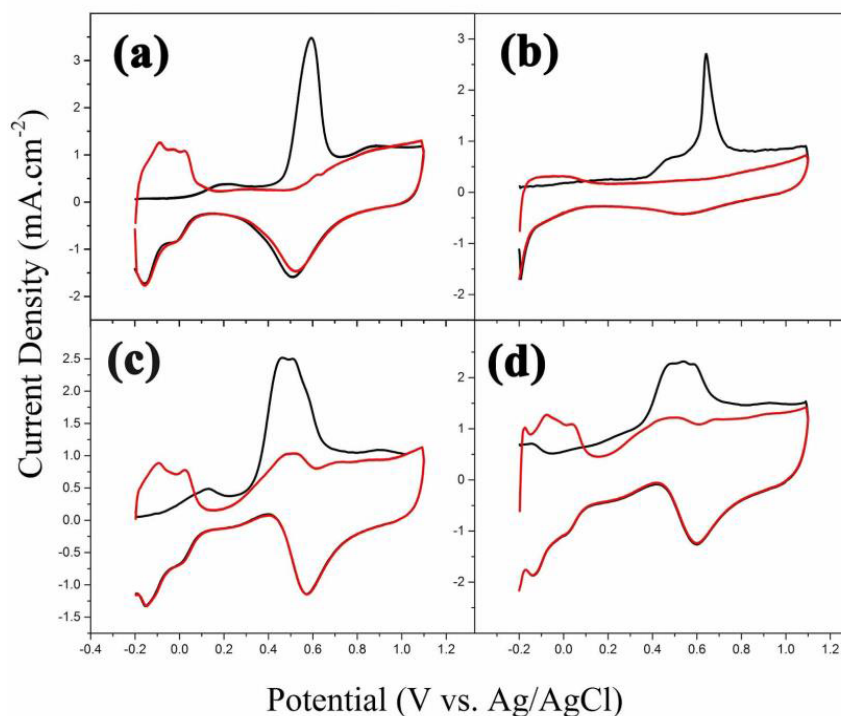


Figure 7. CO-Stripping curves of (a) commercial Pt/C catalyst, (b) Pt/NG-400, (c) Pt/NG-600 and (d) Pt/NG-800 in acidic media. Recorded in 0.5M H₂SO₄, E_{ad}= 0.1 V, Scan rate= 20 mVs⁻¹ [12].

3.2. Oxygen reduction reactions in fuel cells

The oxygen reduction reaction is the primary electrochemical reaction occurring at the cathode of polymer electrolyte fuel cells. Precious metals such as Pt with inherent properties such as high activity and durability in acidic and alkaline electrolytes have been used as catalyst to overcome the disadvantage of slow kinetics of oxygen reduction reactions [13].

In this regard, Aghabarari et al. [14] revealed a significant improvement for oxygen reduction reaction by anchoring Pt nanoparticles (PtNPs) onto a new hybrid chitosan derivative carbon black support. In the approach used, the chitosan derivative was prepared by a Michael reaction with methyl acrylate followed by an amidation reaction with diethylentriamine to obtain chitosan-(N-(2-(2-aminoethylamino)ethyl)propanamide) (CSD). Then, the chitosan derivative obtained was coated on the carbon black (Vulcan XC 72R) with different mass ratios of CSD/carbon (CSD.C) by two different methods to obtain 5 wt% and 10 wt% CSD.C (method 1), and 13 wt% CSD.C (method 2). Method 1 was based on mixing the carbon black dispersed in isopropanol with the appropriate amount of chitosan derivative in 2 wt% acetic acid aqueous solution over 2 h, after which the solvent was removed in a rotary evaporator. Method 2 was used to maximize the amount of biopolymer incorporated by mixing the chitosan derivative in 2 wt% acetic acid aqueous solution with carbon black (mass ratio CSD/carbon = 5/1), dispersing with ultrasonic treatment for 30 min, stirring the mixture at room temperature for 24 h and then separating the obtained CSD.C by centrifugation. Finally, Pt nanoparticles (30 wt%) were anchored onto the hybrid CSD.C by impregnation of an appropriate aqueous solution containing chloroplatinic acid, followed by addition of a NaBH₄ solution to reduce the metal at room temperature. According to Figure 8, the half-

wave potentials of the Pt.5.CSD, Pt.10.CSD, Pt.CSD.M2 and Pt/C (JM) are 0.86, 0.85, 0.84 and 0.85 V, respectively. The onset potential for the oxygen reduction reactions in the chitosan-based catalysts is approximately 20 mV lower than commercial catalyst and does not shift suggesting that the nature of the active site has not changed. Therefore, the results exhibit that the chitosan-based catalysts possess a better performance than the commercial catalyst. Based on the ring current generated from the oxidation of H₂O₂, we can see that both the Pt.CSD.M2 and commercial catalyst produced a lower level of H₂O₂ than the Pt.5.CSD and Pt.10.CSD catalysts.

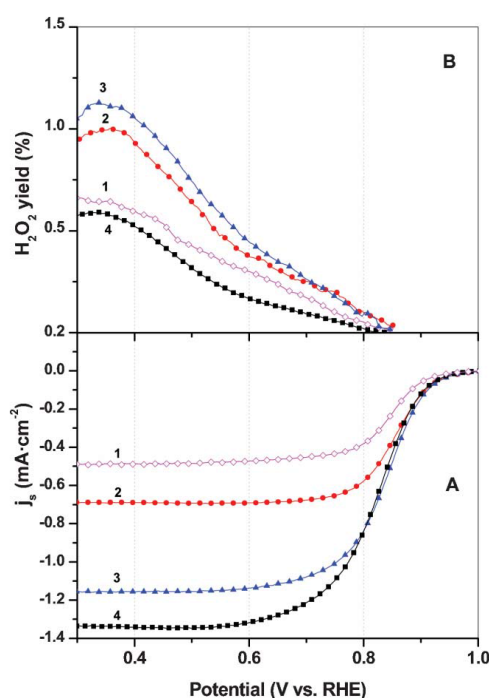


Figure 8. Polarization curves on (A) a glassy carbon rotating ring-disk electrode and (B) H₂O₂ yield of Pt/C (JM) (1), Pt.5.CSD (2), Pt.10.CSD (3) and Pt.CSD.M2 (4).

In order to reduce the costs and realize sustainable development, Aghabarari et al. [13-15] developed bio-nanocomposites of chitosan with graphene and heteropolyacid for oxygen reduction reactions in alkaline media. They proposed a facile and non-precious metal catalyst approach and synthesized nitrogen doped carbon by using melamine and chitosan as low-cost nitrogen source. Further, they prepared hybrid N-based composites by adding heteropolyacid $H_3PMo_{12}O_{40}$ (HPMo) and different transition metals (Fe, Co, Cu). They investigated the electro-catalytic oxygen reduction reaction activities of the composites by using three electrodes set up utilizing cyclic voltammetry and rotating disc electrode in alkaline environment. According to Figure 9, the oxygen reduction reaction activity presents the following order: Fe/HPMo/MeCS > Co/HPMo/MeCS > Cu/HPMo/MeCS. Composites of Fe exhibited the best performance while Cu-composites showed the lower activity. Indeed, nitrogen-doped carbon with transition metals such as Fe or Co improves catalytic activity for oxygen reduction reaction in alkaline electrolyte. Besides, the presence of the heteropolyacid HPMo can improve the activity of chitosan composites.

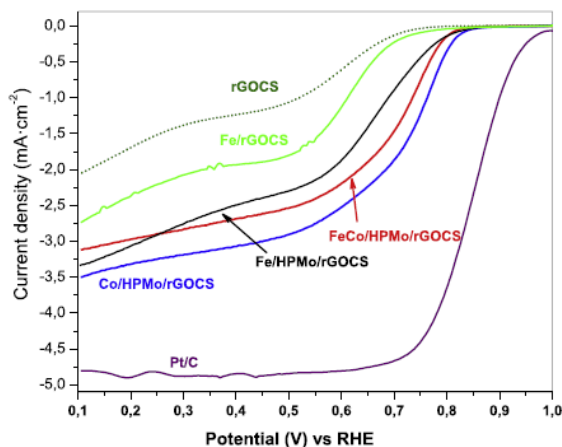


Figure 9. Oxygen reduction reaction of composites recorded in O_2 saturated 0.1 M NaOH solution with a rotation speed of 1600 rpm and potential scan rate of 0.01 Vs⁻¹ [13].

3.4. Corrosion resistant nanocomposite coatings

Polymer coatings are widely used in various industries for enhancing the corrosion resistance of metallic structures. However, these organic coatings could not provide long term corrosion protection due to presence of cracks and defects in the coatings beside their hydrolytic degradation upon exposure to corrosive environment. In order to enhance the life time of polymer coatings, carbon based nanomaterials with outstanding inherent properties have attracted a great deal of attention. In this regard, Pourhashem et al. [16] considered the effect of graphene oxide on corrosion resistant properties of solvent based epoxy coatings, revealing that epoxy coatings containing graphene oxide show significantly higher corrosion resistance compared to pure epoxy samples. They showed that by adding graphene oxide directly to polymer with lower viscosity (hardener or resin), the graphene oxide nanosheets can be dispersed

uniformly in coating matrix. Besides, the wt.% of nanofiller has great effect on dispersion quality and therefore, on corrosion protection performance of coatings. In this study, best corrosion protection was obtained by adding 0.1 wt.% graphene oxide to low viscosity hardener, followed mixing by epoxy resin.

Further, Pourhashem et al. [17] used different silane coupling agents such as 3-aminopropyl triethoxysilane (APTES) and 3-glycidyloxypropyl trimethoxysilane (GPTMS) with amine and epoxy end-groups, respectively, for functionalizing the surface of graphene oxide. According to electrochemical impedance spectroscopy results in Figure 10, that both epoxy/APTES-GO and epoxy/GPTMS-GO nanocomposite coatings (containing 0.1 wt.% nanofiller) showed superior corrosion resistance than epoxy/GO and pure epoxy coating which is due to the positive effect of silane agent on enhancing the interfacial interaction between modified GO sheets with polymer matrix. Their results revealed that the adhesion strength of epoxy coatings to metallic substrates and the water contact angle on epoxy coatings increases by incorporating silane modified GO nanosheets. The improved properties are due to functionalization of GO sheets with silane agents which prevents GO agglomeration in coating matrix, leading to increase of diffusion path for corrosive agents into the coating. Also, the presence of Si-O-Si and Si-O-C bonds within polymer matrix is another parameter for improving the corrosion resistance and bonding strength of nanocomposite coatings. Meanwhile, since the silane functionalized GO sheets are directly added to polyamide hardener with low viscosity, epoxy coatings containing APTES modified GO sheets showed higher corrosion resistance than epoxy/GPTMS-GO nanocomposite coatings; this behavior could be attributed to chemical compatibility between the amine end groups of APTES with polyamide hardener.

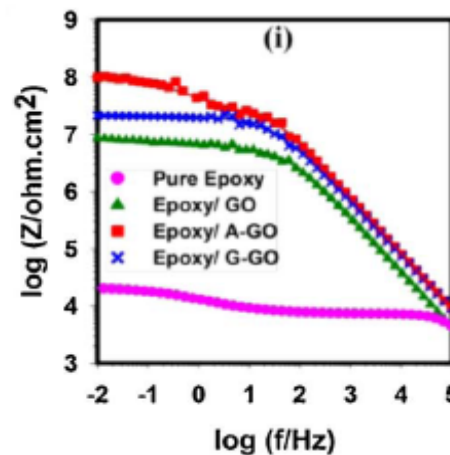


Figure 10. Bode plots derived from electrochemical impedance spectroscopy for pure epoxy, epoxy/GO, epoxy/APTES-GO and epoxy/GPTMS-GO nanocomposite coatings after 14 days of immersion in 3.5 wt.% NaCl solution.

Since epoxy coatings loaded with 0.1 wt.% APTES-GO nanosheets showed higher corrosion resistant than epoxy/GO and epoxy/GPTMS-GO nanocomposite coatings, Pourhashem et al. [18] considered the effect of APTES-GO wt.% (0.05, 0.1, 0.3, and 0.5 wt.%) on corrosion protection performance of epoxy coatings. As presented in Figure 11, epoxy coatings loaded with 0.1 wt.% APTES-GO nanosheets showed the highest corrosion resistance and by increasing the amount of nanofiller in coating matrix, the agglomeration of nanosheets happens; leading to development of pores in the coating and decrease of corrosive agents diffusion path in the coating.

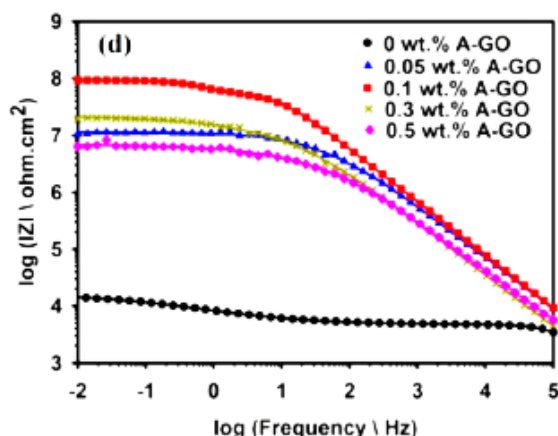


Figure 11. Bode plots for epoxy coatings containing different loadings of APTES-GO (0, 0.05, 0.1, 0.3, and 0.5 wt.%) after 7 days of immersion in 3.5 wt.% NaCl solution.

Moreover, Pourhashem et al. [19] investigated the effect of GO nanosheets decorated by SiO₂ nanoparticles on corrosion protection performance of epoxy coatings. In this research, SiO₂ nanoparticles were synthesized in situ by hydrolysis of tetraethyl orthosilicate on GO sheets. The electrochemical results (Figure 12) demonstrate that SiO₂-GO nanohybrid is promising nanofiller for increasing the corrosion resistance of epoxy coatings. The synthesized nanohybrid can uniformly be dispersed in polymer matrix and increase the barrier performance of epoxy coatings. The presence of active silane groups on the surface of SiO₂-GO nanosheets provides high compact polymer coatings with limited defects and pores.

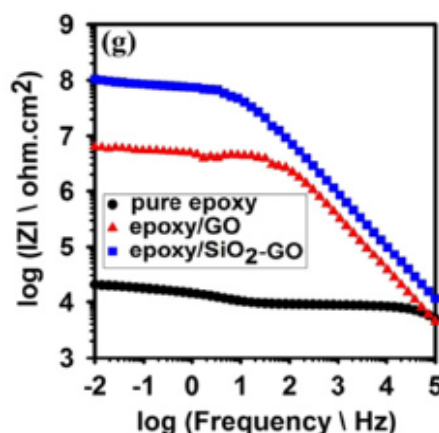


Figure 12. The bode plots of pure epoxy, epoxy/GO and epoxy/SiO₂-GO coatings after 28 days of immersion in 3.5 wt.% NaCl solution.

Conclusion

Carbon nanotubes and graphene nanosheets with significant electrical, chemical, physical, mechanical and thermal properties are candidate for developing the properties of materials. By selecting appropriate treatment methods, these carbon nanomaterials can be used in various fields. Our studies have shown that carbon nanotubes are an excellent option for ammonia gas sensors and supercapacitors. Moreover, the potential application of graphene and its derivatives in drug delivery systems, fuel cells, and anti-corrosion coatings have been demonstrated. This review article would pave the way for other researchers and outlines the great potentials of these carbon nanomaterials.

References

- [1] D.M. Sun, C. Liu, W.C. Ren, H.M. Cheng, "A review of carbon nanotube- and graphene- based flexible thin-film transistors", *Small* 9 (8) (2013) 1188-1205.
- [2] D. Janas and K.K. Koziol, "A review of production methods of carbon nanotube and graphene thin films for electrothermal applications", *Nanoscale* 6 (2014) 3037-3045.
- [3] W.W. Liu, S.P. Chai, A.R. Mohamed, U. Hashim, "Synthesis and characterization of graphene and carbon nanotubes: A review on the past and recent developments", *Journal of Industrial and Engineering Chemistry* 20 (2014) 1171-1185.
- [4] F. Goudarzi, M.R. Vaezi and A. Kazemzadeh, "A novel single wall carbon nanotubes-based sensor doped with lithium for ammonia gas detection", *Journal of Ceramic Processing Research* 13 (5) (2012) 612-616.
- [5] L. Nikzad, M.R. Vaezi, and B. Yazdani, "Synthesis of carbon nanotube-Poly aniline nano composite and evaluation of electrochemical properties", 2nd International Conference on Ultrafine Grained & Nanostructured Materials (UFGNSM) International Journal of Modern Physics: Conference Series 5 (2012) 527-535
- [6] H. Wang, T. Maiyalagan, X. Wang, "Review on recent progress in nitrogen-doped graphene: Synthesis, characterization, and its potential applications", *ACS Catalysis* 2 (2012) 781-794.
- [7] R. Farazi, M.R. Vaezi, M.J. Molaei, M. Saeidifar, "The effect of pH and temperature on the doxorubicin hydrochloride release from magnetite/graphene oxide nanocomposite", International Conference/Workshop of Inter-Islamic Network on Nanotechnology (INN): Nanotechnology and Nanomedicine (2017).
- [8] M. Roca-Ayats, G. García, J. L. Galante, Miguel A. Peña, and M. V. Martínez-Huerta, "TiC, TiCN, and TiN Supported Pt Electrocatalysts for CO and Methanol Oxidation in Acidic and Alkaline Media", *The Journal of Physical Chemistry C* 117(40) (2013) 20769-20777.
- [9] E. Yli-Rantala, A. Pasanen, P. Kauranen, V. Ruiz, M. Borghei, E. Kauppinen, A. Oyarce, G. Lindbergh, C. Lagergren, M. Darab, S. Sunde, M. Thomassen, S. Ma-Andersen, E. Skou, "Graphitised carbon nanofibres as catalyst support for PEMFC", *Fuel Cells* 11 (6) (2011) 715-725.

[10] D.Y. Chung, K.J. Lee, and Y.E. Sung, "Methanol electro-oxidation on the Pt surface: revisiting the cyclic voltammetry interpretation", *The Journal of Physical Chemistry C* 120 (17) (2016) 9028-9035.

[11] M.A. Asghari, B. Aghabarari, M. Javaheri, H. Ghadamian, M.V. Martinez-Huerta, "A comparison between different novel carbon supported platinum nano-catalysts for methanol oxidation reaction", 13th Annual Electrochemistry Seminar of Iran (2017).

[12] M.A. Asghari, B. Aghabarari, M. javaheri, H. Ghadamian, M.V. Martinez-Huerta, "Synthesis of N-doped graphene Based Platinum nanoparticles as anode catalyst for use in direct methanol fuel cell", 6th International Conference on Materials Engineering and Metallurgy (2017).

[13] B. Aghabarari, Z. Afzali, M.C. Cápel-Sánchez, M Jesús Lázaro, M. V. Martínez-Huerta, "Effect of transition metals on the structure and activity of the melamine/chitosan composites for oxygen reduction reaction", *Proceedings of the 7th International Conference on Nanostructures (ICNS7)* (2018), Iran.

[14] B. Aghabarari, M. V. Martinez-Huerta, M. Ghiaci, J. L. G. Fierro and M. A. Pena, "Hybrid chitosan derivative-carbon support for oxygen reduction reactions", *RSC Advances* 3 (2013) 5378-5381.

[15] B. Aghabarari, N. Nezafati, M. Roca-Ayats, M.C. Capel-Sanchez, M.J. Lazaro, M.V. Martinez-Huerta, "Effect of molybdophosphoric acid in iron and cobalt graphene/chitosan composites for oxygen reduction reaction", *International Journal of Hydrogen Energy* 42 (2017) 28093-28101.

[16] S. Pourhashem, M.R. Vaezi, A.M. Rashidi, M.R. Bagherzadeh, "Exploring corrosion protection properties of solvent based epoxy-graphene oxide nanocomposite coatings on mild steel", *Corrosion Science* 115 (2017) 78-92.

[17] S. Pourhashem, A.M. Rashidi, M.R. Vaezi, M.R. Bagherzadeh, "Distinctive roles of silane coupling agents on the corrosion inhibition performance of graphene oxide in epoxy coatings", *Progress in Organic Coatings* 111 (2017) 47-56.

[18] S. Pourhashem, A.M. Rashidi, M.R. Vaezi, M.R. Bagherzadeh, "Excellent corrosion protection performance of epoxy composite coatings filled with amino-silane functionalized graphene oxide", *Surface and Coatings Technology* 317 (2017) 1-9.

[19] S. Pourhashem, M.R. Vaezi, A.M. Rashidi, "Investigating the effect of SiO₂-graphene oxide hybrid as inorganic nanofiller on corrosion protection properties of epoxy coatings", *Surface and Coatings Technology* 311 (2017) 282-294.

Evaluation and optimization of supercritical extraction of insulin from *Otostegia persica*

N. Nourinasab, S.M. Ghoreishi*, S.S. Banifatemi

Dept. of Chem. Engineering, Isfahan University of Technology, Isafahan, 84156-83111, Iran
*Corresponding Author: e-mail: ghoreshi@cc.iut.ac.ir; phone: +98-31-33915604

Abstract

In this study, the extraction of insulin from *otostegia persica* was enquire by Soxhlet extraction and modified supercritical CO₂ with methanol as solvent and 30 min of static time. Design of experiment was executed with response surface methodology (RSM) using Mini Tab software 17. The operating temperature (40–60°C), pressure (15–35 MPa), dynamic extraction time (60–120 min) and CO₂ flow rate (0.8–2 ml/min) were regarded as the range of operating variables UV test was applied to recognize and quantitatively determine the amount of extracted insulin. Response surface analysis proved that R₂ and modified R₂ of the model were 98.16% and 96.54%, respectively. The RSM modeling prophesy the optimal operating conditions to be the pressure of 28.1 MPa, temperature of 47°C, CO₂ flow rate of 2 ml/min and dynamic extraction time of 109 min in which the maximum absorption coefficient of 0.7.

Keywords: Supercritical extraction, Insulin, Optimization, Response Surface Methodology, *Otostegia Persica*.

1. Introduction

Otostegia persica is native of Iran, Pakistan and Afghanistan that widely distributed in southern and southeastern Iran. In traditional Iranian medicine, this herb is used to treat diabetes, fever, malaria and toothache. Also, in clinical and experimental studies, there have been cases of relief, arthritis effects and anti-inflammatory peroxidation.

In addition, the hydro alcoholic extract improves the leave morphine syndrome. It has been reported that polyphenolic antioxidants in some plants are useful in the improvement of diabetes complications. *Otostegia persica* has polyphenols polar compounds such as Flavonoids and Tannins. Flavonoids usually do their antioxidant activity by combining with free radicals. It has been reported that methanolic extract of the *o.persica* has an antioxidant activity that has a beneficial role in the improvement of diabetes mellitus also *o.persica* has a hypoglycemic effect that is shown by improving the pancreatic islets and increasing insulin secretion [1,2].

According to the study, the methanolic extract of this plant has strong antioxidant activity due having of Morin and Quercetin flavonoids and prevents the destruction of DNA cells. Quercetin is able to collect xanthine superoxide and xanthine oxide radicals. This flavonoid is beneficial through reducing oxidative stress on improving the difficulty of the vessels and cataracts caused by diabetes. A series of studies show that this flavonoid is able to increase serum levels of insulin and calcium in the blood. In general,

flavonoid Morin in plants of the family moraceae is non-toxic and has antioxidant, anti-allergic, anti-inflammatory, anti-mutagenic and anti-cancer effects. In addition to the activity of collecting free radicals, Quercetin in the *o.persica* also has the ability to inhibit pancreatic lipase. Flavonoids do from several procedures themselves antioxidant actions. For example, combining with free radicals and producing less active products, inhibiting metabolic enzymes such as lipoxygenase, cyclooxygenase, xanthine oxidase and nitric oxide synthase, which are involved in the production of free radicals. It has also been shown that flavonoids Morin and Quercetin oppose cholesterol oxidation. Generally, this plant probably reduces serum glucose by reducing free radicals and improving pancreatic islets and increasing insulin levels [3,4].

The main objective of this study was insulin extraction from *o.persica* by modified SC-CO₂ in periodic static-dynamic method for pharmaceutical application. The optimization was performed by response surface methodology (RSM). The RSM is beneficial for modeling, problem analysis and optimization when a response (i.e., extraction recovery) is influenced by several variables such as pressure, temperature, flow rate of SC-CO₂ and dynamic time. In this work the other impressive variable (static time) was fixed at optimum value of 30 min that was procure by experiment.

The methods used to extract this substance are all inclusive solvent-extracted, which, on the other hand, are not cost-effective due to the high consumption of energy and solvent and On the other hand, the provision and recovery of solvents that are very important in food and medicine is not entirely possible. Organic solvents, especially chlorinated solvents, are harmful for environment. This problem has been resolved by replacing CO₂ as the most common solvent in supercritical processes because carbon dioxide is cheap, it has a low critical temperature and pressure, non-explosive, non-toxic and non-reactive properties, and it is also safe for the environment [5-8].

2. Experimental

2.1. Materials

O.persica was prepared from Kerman co. The samples were screened with mesh size of 20–35 (0.841–0.507 mm). Methanol (purity ≥ 99.9%, Merck), deionized water and industrial grade carbon dioxide (purity > 99%) were utilized for Soxhlet and supercritical fluid extraction and UV test.

2.2. Soxhlet extraction

For Soxhlet extraction, 1 g of o.persica in a filter paper set in a Soxhlet device and then continued extraction for 8 hrs. and methanol was used as solvent. After this work, the solvent was vaporized by rotary vacuum evaporator (30°C), and the extract was dried at 70°C to delete remaining solvent to required amount. Then the amount of insulin was determined by UV test. The absorption coefficient obtained from the extraction of Soxhlet was 0.7 which is considered as a 100% extraction.

2.3. Supercritical fluid extraction: devices and procedure

To do this study, the supercritical extraction system shown in Fig. 1 was used.

2.3.1. CO₂ cylinder

The cylinder is intended to store carbon dioxide. There is a pipe to transfer carbon dioxide to the end of the tank. Its degree of purity is usually higher than 97%.

2.3.2. Molecular sieve

A molecular sieve is intended to dry out and increase the degree of purity of carbon dioxide gas. The sieve consists of a tube filled with molecular sieve K28751105148-sieve5A.

2.3.3. Cooler circulator

A cooler is used to convert carbon dioxide into a liquid before entering the pump. In these coolers, ethylene glycol is usually used as a cooling agent.

2.3.4. High pressure pump

High pressure liquid chromatography pumps are used to pump the solvent into the extraction vessel. The solvent present in the tank is pressurized by the pump about 3750 to 10000 psi.

2.3.5. Needle valve

In order to control the input of carbon dioxide and to save carbon dioxide, one valve is placed at the pump outlet.

2.3.6. Oven

Ovens work with airflow and are commonly used to control and maintain the temperature of the chromatography column. The temperature range is from -15 °C below ambient temperature to 80 °C.

2.3.7. Extraction cell

The extraction cells in the SFE range from 10 to 200 milliliters and are mostly of stainless steel 316 or other similar resistant materials. The temperature control is usually done by placing the sample cells in the oven.

2.3.8. Back pressure regulator

The pressure of the system by the back pressure of the back pressure regulator not only ensures the back pressure, but also controls the flow rate of the fluid flowing through the system.

The Tescom Series 24-1762-26 was used in the project. The maximum and minimum pressure of this regulator is 414 and 34 bar, and the maximum operating temperature of this device is 204.

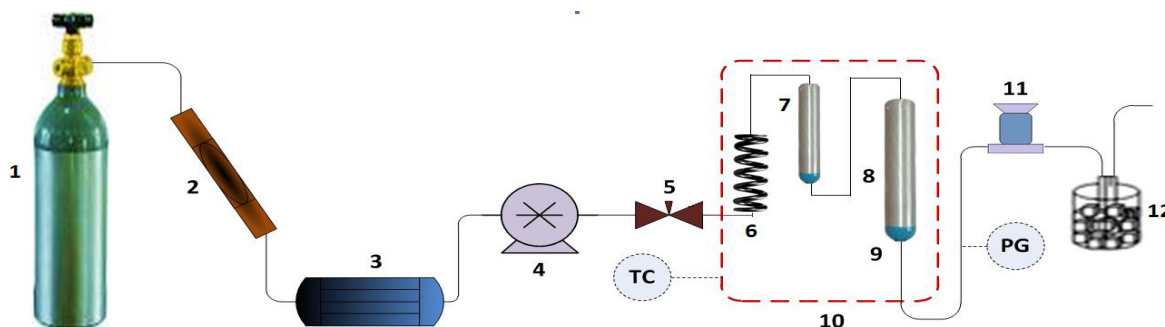


Figure 1. Schematic diagram of experimental setup for the supercritical extraction system; (1) CO₂ cylinder, (2) column consisting of molecular sieve and silica gel, (3) chiller, (4) pump head cooler, (5) HPLC pump, (6) needle valve, (13) BPR valve, (14) extracted sample collection vessel.

2.4. UV test

We first turn on the device and wait for it to start up. Then we set the wavelength of the device to 400 to 700 according to the standard method in order to determine the absorption factor to represent the required factor. The deionized water poured in the cell and added reactive and entered the device. Calibrate the device and then read the absorption coefficient of each sample.

3. Design of experiment

Traditionally, optimization has been executed by checking the impression of one factor at a time on response. In other words, just one parameter is

investigated while others are saved at a constant level. The main disadvantages of this optimization method were (1) a large number of experiments that need to be done require time and cost and (2) the interactive effects between distinct operating variables are not considered. To solve these problems, the optimization was executed by using multi-variants statistic methods such as Response Surface Methodology (RSM). RSM method is combination of mathematical and statistical techniques that when a response is influenced by several variables are beneficial for solve modeling and analysis subjects. In order to obtain the best answer, simultaneously optimize the levels of these variables.

The steps in this procedure are as follows:

1. Select the variables that have the most impact on the response. Identify the variables that may affect the response. Therefore, it is necessary to pick out those variables with main effects.
2. Choose the experimental design and executed according to the selected experimental matrix and getting answers.

RSM model is shown in Eq (1):

$$Y = A_0 + \sum_{i=1}^k A_i Z_i + \sum_{i=1}^k A_{ii} Z_i^2 + \sum_i \sum_j A_{ij} Z_i Z_j + \varepsilon \quad (1)$$

Where, A_0 is Regression coefficient for constant coefficient, A_i is Regression coefficient for linear terms, A_{ii} is Regression coefficient for square terms, A_{ij} is Regression coefficient for interactions terms, ε is A collection of statistical errors that are not covered by the main part of the function and k is the number of variables.

In RSM, the central composite design (CCRD) is usually used to determine how the tests are performed. In this case, prior to the design, the selected levels are encoded. The central value of the code is zero, smaller numbers get negative code and bigger numbers get positive code in which these codes are integers. To calculate the actual values of the parameters at the coded levels according to the following equation:

$$Z_i = \frac{X_i - X_{i,c,p}}{\Delta_i^\xi} \quad (2)$$

Where Z_i is code for each level, X_i is the value of the parameter in the maximum, minimum or center point, $X_{i,c,p}$ is the value of the parameters in the center point and ξ is the value of the distance between X_s in the maximum, minimum or central points.

Coded Levels	Temperature [°C]	Dynamic time [min]	Pressure [Mpa]	Flow rate [ml/min]
-2	40	60	150	0.8
-1	45	75	200	1.1
0	50	90	250	1.4
1	55	105	300	1.7
2	60	120	350	2

Table 1. Uncoded and coded levels of independent variables used in the RSM design.

3) Detect a suitable model of the response variables according to the fit of a polynomial equation to the experimental data. After catching data linked to each experimental point, it is necessary to fit a mathematical equation to qualify the behavior of the response to the levels of studied values. In other words, the coefficients of Eq. (3) are acquired via least square method (LSM). LSM is a multiple regression technique with generating the lowest residual possible that used to fit a mathematical model to a collection of experimental data.

4) The evaluation of the model's validity. The attained mathematical model was appraised by the application of analysis of variance (ANOVA), coefficient of determination (R^2), and adjusted coefficient of determination (Adj. R^2).

5) Finding the optimum values of model for each variable that studied. Finally, the needful conditions were determined for optimum recovery of insulin extraction through the first derivative of the mathematical function, which depicts the response surface [9,10].

Between the several experimental design methods, RSM was chosen in this reading to specify the effects of pressure, temperature, flow rate and dynamic time in binary modifier on the extraction efficiency of insulin. Therefore, four levels central composite rotatable design (CCRD) was used with four independent variables.

The independent variables in this study were dynamic time (t), flow rate of SC-CO₂ (Q), temperature (T), pressure (P), in the range of 60–120 min, 0.8–2 ml/min, 40–60°C, 15–35 MPa, respectively. Recovery of insulin extraction was response variable (dependent variable). The Table 1 shows the coded and uncoded levels of independent variables and Table 2 also shows 31 experimental runs that are according to coded levels of the independent variables in the CCRD for performance of RSM used from Minitab17.

Number of experiments	(p)	(T)	(t)	(Q)	Absorb
1	-1	-1	-1	-1	0.4982
2	0	0	0	0	0.5435
3	1	1	-1	-1	0.54
4	0	0	0	0	0.5452
5	-1	-1	-1	1	0.5417
6	0	0	2	0	0.5640
7	1	1	1	1	0.5550
8	1	-1	-1	1	0.5375
9	0	0	0	-2	0.4773
10	0	0	0	0	0.5445
11	-1	-1	1	1	0.5648
12	1	1	1	-1	0.5042
13	0	0	0	0	0.5337
14	0	2	0	0	0.5032
15	1	-1	-1	-1	0.4880
16	0	0	0	0	0.5489
17	0	0	0	0	0.5487
18	0	0	0	0	0.5383
19	1	-1	1	1	0.5641
20	-1	1	-1	-1	0.4089
21	-1	1	1	1	0.5315
22	0	-2	0	0	0.5647
23	-2	0	0	0	0.4485
24	-1	-1	1	-1	0.5311
25	0	0	0	2	0.5676
26	2	0	0	0	0.5117
27	-1	1	1	-1	0.4669
28	1	1	-1	1	0.5185
29	-1	1	-1	1	0.4871
30	1	-1	1	-1	0.5268
31	0	0	-2	0	0.4919

Table 2. Results obtained from supercritical extraction of insulin.

4. Results and discussion

4.1. Fitting the model and analysis of experimental data

The experimental data available in Table 2 are used to obtain the coefficients of the second-order polynomial equation (Equation (5)) by the LSM. The regression anomalies are summarized in Table 3 and the value of each coefficient is determined based on the absolute value of t and the value of p in the table. For any of the terms in the model, a large absolute value of t and a small p -value would represent more notable effects on the corresponding response variables. In this project, the parameters with $p < 0.001$ as parameters are very important and effective and Parameters with $p < 0.01$ as important parameters and Parameters with a p value of more

than 0.05 are known as parameters that do not have a significant effect. The second-order polynomial model was required for insulin recovery (R) as a function of independent variables in Eq. 3.

According to Table 3, the terms of pressure, temperature, dynamics time and flow rate were very important and highly significant from quadratic terms p^2 and t^2 were highly significant and other parameters were not important. The calculated coefficient of determination (R^2) and adjusted coefficient of determination (Adj. R^2) were 98.16% and 96.54%, respectively that which indicates the appropriate accuracy of the proposed model for the fitting of experimental data in a statement that about 98% of the changes are covered by the model.

$$R = 29.506 + 2.501p + 1.883T + 1.840Q + 1.022t - 0.573p^2 - 0.457T^2 + 0.297Q^2 - 1.649t^2 - 0.123Pt + 0.402PQ - 0.137pt + 0.263TQ - 0.078Tt + 1.034Qt \quad (3)$$

4.2. Optimization of extraction operating conditions

Because there is no unique answer to designing a process, a design can include several designs, so choosing the best one from the available options is of particular importance. Optimization emphasizes the better the solution to a problem and tries to move the optimal solution by changing a basic idea. This path of motion may reach the optimal answer or be near optimum. Therefore, optimum conditions of the experiment were obtained at temperature of 47°C, pressure of 28.1 MPa, flow rate of 2 ml/min and dynamic time 109 min.

4.3. Response surface analysis

The interactions among different variables and optimum values for reaping the maximum recovery by a three-dimensional response surface model according to Eq. (5) were perused.

The best way to examine the effect of operating parameters on the rate of recovery of insulin is to plot the response surface diagrams in a three or two dimensional. In these plot, the axis A is designed for the response, and the axis B and P for the two independent variables and two other variables are zero (central point). In Fig. 2, the effect of pressure and temperature on insulin recovery is shown that in this figure Dynamic time and flow rate are 90 min and 2 ml/min, respectively.

The effect of the pressure parameter can be explained this way that the pressure and density of carbon dioxide are directly related to each other, with increasing pressure, the density of carbon dioxide increases. With increasing density, the molecular distance decreases and As a result, the molecular interactions between the solvent and the extract increase Which increases the supercritical

fluid solubility And it has a positive effect on the recovery rate of the extract as it increases recovery, It should be noted that increasing pressure also has a negative effect on recovery And it decreases with increasing pressure, diffusivity and mass transfer coefficient [11, 12]. As shown in Figure 2, the increase in pressure initially increases the recovery rate and from a pressure of 28 up the recovery rate is reduced because repulsion increases between the solvent and the soluble component. In fact, it can be said that when pressure ranges from 15 to 28, the increase in carbon dioxide density is dominant and from the 28th onwards, the reduction of the mass transfer coefficient and the reduction of diffusivity are predominant. Flow rate and dynamic time are 1.4 ml/min and 90 min respectively, which are the same central points. As shown in Table 4, the pressure has a positive linear effect ($p < 0.001$) on the rate of recovery of insulin at low pressure levels that it's due to the increased carbon dioxide density because of the high pressure. At high pressures, the negative effect of the squared pressure parameter ($p < 0.001$) is also significant and with increasing pressure, as already said, the recovery rate is reduced which is due to increased repulsion between the solvent and the soluble component at high pressures and the reduction of diffusivity and mass transfer coefficient.

Regarding the effect of the temperature parameter, it can be said that this parameter can have both negative and positive effect. Increasing the temperature increases the density that this reduces the solvent of solubility power and thus reduces the recovery rate. The increase in temperature also increases the vapor pressure of the components which increases the solubility of the extract in supercritical carbon dioxide. What effect the temperature has on the recovery rate depends on which one has a dominant effect [13, 14].

term	coefficient	T-value	p-value
A ₀	29.506	107.76	0.000
P	2.501	16.92	0.000
t	1.022	6.91	0.000
T	1.883	12.73	0.000
Q	1.84	-12.85	0.000
P ²	-0.573	-4.23	0.001
t ²	-1.649	-12.17	0.000
T ²	-0.457	-3.37	0.004
Q ²	0.297	-2.19	0.044
P×t	-0.137	-0.76	0.461
P×T	-0.123	0.68	0.506
P×Q	0.402	2.22	0.041
t×T	-0.078	-0.43	0.672
t×Q	1.034	5.71	0.000
T×Q	0.263	1.45	0.166
R ² =98.16% , R ² (adj)= 96.54%			

Table 3. Regression coefficients of predicted second-order polynomial model for insulin recovery.

Source	Degree of freedom	Sum of squares	Mean square	f-value	p-value
Model	14	447.214	31.944	60.87	0.000
Linear	4	341.602	85.400	162.74	0.000
P	1	150.150	150.150	286.13	0.000
T	1	25.072	25.072	47.78	0.000
T	1	85.089	85.089	162.15	0.000
Q	1	81.291	81.291	154.91	0.000
Square	4	84.161	21.04	40.09	0.000
P ²	1	9.382	9.382	17.88	0.001
T ²	1	77.761	77.761	148.18	0.000
T ²	1	5.960	5.960	11.36	0.004
Q ²	1	2.514	2.514	4.79	0.044
Interactions	6	21.451	21.575	6.81	0.001
P×T	1	0.3	0.3	0.57	0.461
P×T	1	0.243	0.243	0.46	0.506
P×Q	1	2.584	2.584	4.92	0.041
T×T	1	0.098	0.098	0.19	0.672
T×Q	1	17.119	17.119	32.62	0.000
T×Q	1	1.108	1.108	2.11	0.166
Error	16	8.369	0.525	-	-
Lack of fit	10	6.375	0.638	1.89	0.225
Pure Error	6	2.021	0.337	-	-
Total	30	455.610	-	-	-

Table 4. ANOVA of RSM modeling for insulin recovery.

As shown in Fig. 2, the recovery rate is reduced by increasing the temperature. In fact, it can be said that when the temperature ranges from 40 to 47, the recovery rate is very good and decreases from 47 up. Table 4 also confirms these effects with a negative coefficient by having a positive effect for the linear term of the temperature and the negative effect for the temperature term ($p < 0.001$). The effect of this parameter is that the increase in flow rate causes reduction of the thickness of the film layer around solid particles and increases the film mass transfer coefficient which overcomes the mass transfer resistance and also the common surface resistance regarding the transfer of the soluble component from the sample matrix [15]. As shown in Fig. 3, with increasing flow rate the recovery rate increases at constant temperature which is due to the reduction of film thickness layer around solid particles and the

mass transfer resistance. In these figure, the values of the pressure and temperature parameters are 25 MPa and 50 respectively. As shown in Table 3, this parameter has a positive effect on the recovery rate. During the dynamic time, the new solvent passes through the samples. As long as there would have existed effective propulsion between the fresh fluid and the sample for mass transfer increasing the dynamics time increases insulin recovery. As shown in Fig. 5, the dynamic time increases, the insulin recovery rate also increases. As shown in Table 3, the extraction time has a positive linear effect on recovery rate of insulin ($p < 0.001$). By increasing the extraction time, the negative effect of square term time ($p < 0.001$) has also been important and this increase, after 120 minutes, will not have much effect on the recovery rate.

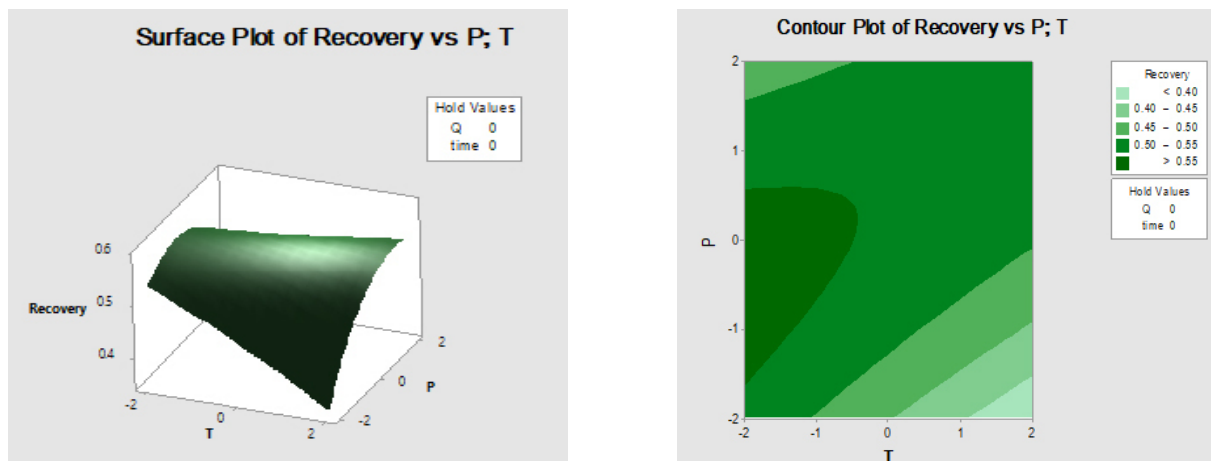


Figure 2. Surface and contour plots of recovery versus P and T.

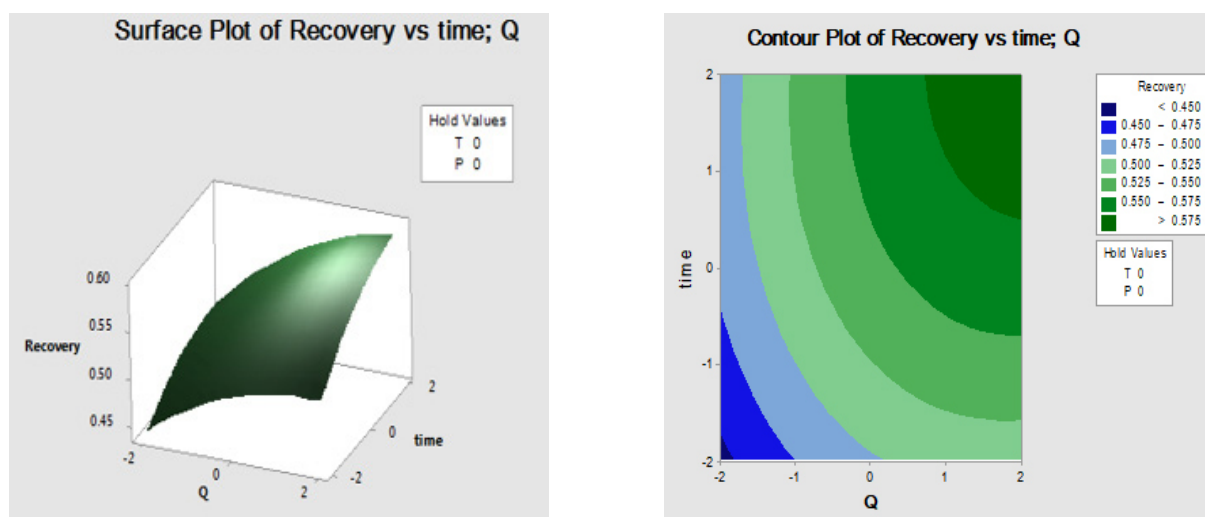


Figure 3. Surface and contour plots of recovery versus time and Q .

5. Conclusions

In this research, extraction of insulin from the plant was carried out using two different methods of extraction with supercritical carbon dioxide and extraction with Soxhlet. In extraction by Soxhlet with methanol solvent, the time of 8 hours was chosen. Also, the RSM to the most appropriate operating conditions for the extraction of insulin, pressure 28 Mpa, temperature 47, flow 2 ml/min, and dynamic time dynamics 109 min predicted. In general identified that the linear terms of pressure and time are very important this is while carbon dioxide flow rate is of relatively high importance. The square terms of all variables are also very important except carbon dioxide flow rate.

Acknowledgments

The financial support provided by Isfahan University of Technology is gratefully acknowledged.

References

- [1] Le K, Chiu F, Ng K. Identification and quantification of antioxidants in *Fructus Lycii*. *Food Chem* 2007; 105: 353-363.
- [2] Zargari A. *Medicinal plants*. 2nd edition. Tehran University Publisher, Tehran, 1989.
- [3] Shariffar, F, Yassa, N, Shafiee, A. Antioxidant activity of *Osteoglossum persica* (Labiatae) and its constituents. *Iran J Pharm Res* 2003; 2: 235-239.
- [4] Williamson EM. *Liquorice*. In *Potter's Cyclopaedia of Herbal Medicines*. C W Daniels: Saffron Walden, UK, 2003 269-271.
- [5] Ramsey, E, Sun, Q, Zhang, Z, Zhang, C, Gou, W. Mini-review: green sustainable processes using supercritical fluid carbon dioxide. *Journal of Environmental Sciences*, 2009; 21(6): 720-726.
- [6] Anitescu, G, Tavlarides, LL. Supercritical extraction of contaminants from soils and sediments. *Journal of Supercritical Fluids*, 2006; 38: 167-180.
- [7] Akbari, I, Ghoreishi, SM, Habibi, N. Generation and precipitation of paclitaxel nanoparticles in basil seed mucilage via combination of supercritical gas antisolvent and phase inversion techniques. *J. of Supercritical Fluids* 2014; 94: 182-188.
- [8] Bashipour, F, Ghoreishi, S M. Response surface optimization of supercritical CO₂ extraction of α -tocopherol from gel and skin of Aloe vera and almond leaves. *J. of Supercritical Fluids* 2014; 95: 348-354.
- [9] Debenedetti, PG, Kumar, SK. The molecular basis of temperature effects in supercritical extraction. *Journal of AIChE*, 1988; 34(4): 645-657.
- [10] Sanal, IS, Bayraktar, E, Mehmetoglu, Ü, and Çallımlı, A. Determination of optimum conditions for SC-(CO₂ + ethanol) extraction of β -carotene from apricot pomace using response surface methodology. *Journal of Supercritical Fluids* 2005; 34(3): 331-338.
- [11] Wei, Z.-J., Liao, A.-M., Zhang, H.-X., Liu, J, and Jiang, S.-T. Optimization of supercritical carbon dioxide extraction of silkworm pupal oil applying the response surface methodology. *Journal of Bioresource Technology* 2009; 100(18): 4214-4219.
- [12] Liu, S, Yang, F, Zhang, C, Ji, H, Hong, P, and Deng, C. Optimization of process parameters for supercritical carbon dioxide extraction of *Passiflora* seed oil by response surface methodology. *Journal of Supercritical Fluids* 2009; 48(1): 9-14.
- [13] Ghoreishi, SM, Mardani, E, Ghaziaskar, HS. Separation of γ -linolenic and other polyunsaturated fatty acids from *Boraginaceae* via supercritical CO₂. *Journal of Separation Science* 2011; 34: 233-240.
- [14] Ghoreishi, SM, Bataghva, E. Supercritical extraction of evening primrose oil: experimental optimization via response surface methodology. *Journal of AIChE* 2011; 57(12): 3378-3384.
- [15] Yi, C, Shi, J, Xue, SJ, Jiang, Y, Li, D. Effects of supercritical fluid extraction parameters on lycopene yield and antioxidant activity. *Journal of Food Chemistry* 2009; 113(4): 1088-1094.

Effects of chemical and mechanical functionalization of carbon nanotubes on the behavior of a CNT/Phenolic nanocomposite

M.J. Hadianfard, M. Alizadeh and M. Moradzaman

Department of Materials Science and Engineering, School of Engineering, Shiraz University, Shiraz, Iran
*Corresponding Author: hadianfa@shirazu.ac.ir

Abstract

Carbon nanotubes and their treatments play an important role in fabrication and properties of the nanocomposites. In this study effects of acid functionalization and mechanical treatment of CNTs by ball milling on the chemical structure, weight loss and mechanical strength of a 1 weight % CNTs reinforced phenolic polymer has been investigated by using FTIR, XRD, TGA, electron microscopy and tensile tests. Results show that both chemical and mechanical treatment has considerable effects on properties of the composite. Maximum strength was obtained by chemical treatment followed by 2 hours of mechanical treatment, further milling treatment caused to decrease the strength of the composite.

Keywords: Carbon nanotubes, Nanocomposites, Functionalization, Ball milling, Mechanical properties

Introduction

Carbon nanotubes are widely used for fabrication of nanocomposites [1-4]. Multiwall carbon nanotubes present greater mechanical properties compared to the other carbon materials, in addition, they offer excellent specific strength and stiffness together with low weight and high specific area [2, 5]. Major difficulties in the use of carbon nanotubes in different areas are their hydrophobicity, surface chemistry, a tendency to clustering and building aggregate [6-8]. Functionalization methods are providing techniques for overcoming these barriers and increasing compatibility of carbon nanotubes with other materials. [9,10]. Properties of a composite reinforced with certain amount of CNTs is dependent on several factors such as degree of dispersion of the CNTs in the matrix [8,11], sort and density of the functional groups on the surface of the CNTs, which are controlling type and strength of the CNT/matrix interfaces [12,13] and aspect ratio of the CNTs [14]. Chemical and mechanical functionalization are methods which can manage the degree of dispersion and CNT/matrix interface properties [15] while chemical functionalization methods are studied widely, less attention has been paid to the effects of mechanical functionalization on the properties of a composite reinforced with CNTs. Therefore the main aim of this study is to investigate effects of mechanical treatment with and without chemical functionalization on the mechanical behavior of a composite reinforced with CNTs.

Experimental Procedures

For reinforcement phase multiwall carbon nanotubes (MWCNT) with an average diameter of 15 nm, the

diameter range of 9-21 nm and an average length of 20 μm with 95% purity were purchased.

A thermoset novolac phenolic resin with a particle size of 60 μm with the hardener of hexamethylenetetramine (C₆H₁₂N₄) was used as a matrix of the composite.

For chemical functionalization, the raw CNTs were poured into ethanol alcohol and sonicated for 4 hours. Then 5 gr of the CNTs were added to 250 ml of 0.65 molar nitric acid and heated to 80 C° stirred for 1.5 hours, then the mixture cooled to the room temperature. Next residual nitric acid was removed from the mixture and the CNTs were washed with distilled water for several times until their pH reached 7. After filtration, The CNTs were dried at 70 C° in a vacuum oven for 24 hours and FCNTs were formed.

Mechanical functionalization was performed by mixing the raw CNTs or FCNTs with resin powders and milled with the ball mill for different duration of time ranging from 0 to 6 hours. For this propose a planetary ball mill with powder to ball ratio of 1 to 10, the speed of 50 rpm and ball diameter of 5 mm was used.

Nanocomposite specimens were fabricated by adding 1 wt % raw CNTs or FCNTs to the phenolic resin powders and milled for a designated time to obtain a uniform mixture of the CNTs into the resin. After separation balls, the mixture was poured into a metallic die and cured under pressure of 80 bar and temperature of 180 C° for two hours.

For evaluation effects of chemical and mechanical functionalization, 5 specimens were fabricated from each FCNTs/phenolic and raw CNTs/phenolic with 0, 1, 2, 4 and 6 hours of ball milling.

Thermogravimetric analysis of the specimens was completed in the atmospheric environment by an STA-1500, Rheometric Scientific, USA. For chemical analysis, a Fourier transform infrared spectroscopy (FTIR) was performed by using Nicolet Magna-IR760 FTIR spectrometer. A strength of the specimens was measured by flexural tests according to ASTM D-790 test method on specimens with 2.8×11.2 mm cross-section. Structure of the specimens was evaluated by X-ray diffraction method and electron microscopy.

Results

Figure 1 displays a TEM micrograph obtained from the raw CNTs this figure shows that the CNTs have a large aspect ratio and made bundles with each other. FTIR spectrum of the raw and chemical functionalized multiwall carbon nanotubes are shown in Figure 2. The broad absorption peak at 3433 cm⁻¹ is due to O-H stretching vibration bond [16], this peak can be generated by absorption hydroxyl (O=C-H and C-OH)

groups due to reaction of acid with surface of the CNTs during chemical treatment in functionalization process, it may also be produced due to water absorption by the raw CNTs from environment. Higher absorption of FCNTs at 3433 cm^{-1} wavenumber compared to the raw CNTs is observed in Fig. 2 and exhibits formation of a hydroxyl group on the surface of the FCNTs.

The peaks at 1635 cm^{-1} are formed by vibrational stretching of C=C bond and peaks at 1367 cm^{-1} is due to C-C stretch [17, 18]. Both peaks showing higher absorption in the raw CNTs compared to the FCNTs these differences can be resulted from oxidation of carbon by acid during chemical functionalization process. It seems that introducing functionalities leads to partly distraction of the graphitic surface layer.

Another difference between FTIR spectrum of the raw CNTs and FCNTs appears at 2360 cm^{-1} which is showing higher absorption in the case of FCNTs, This peak formed by vibrational absorption

of C-O-C bonds and confirming the success of the functionalization process.

Small peaks around 1736 cm^{-1} which are only observed for FCNTs are due to carboxyl (COOH) groups. These peaks confirm attachment of carboxyl group to the surface of the CNTs. Peaks between 1150 to 1050 cm^{-1} which are observing stronger in the spectra of FCNTs are representing a stretch of C-O bond in the hydroxyl group



Figure 1. TEM micrograph obtained from raw CNTs.

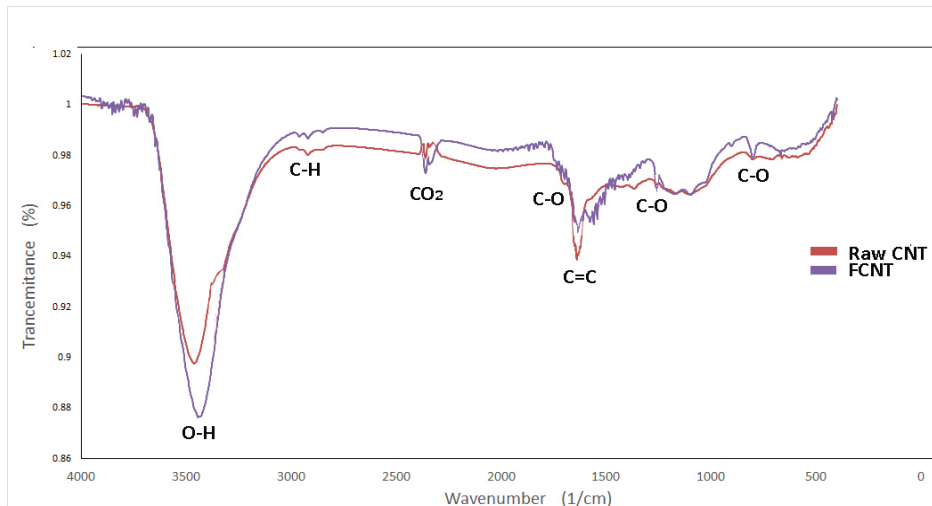


Figure 2. FTIR spectrum from the raw and chemical functionalized CNTs.

FTIR spectra of the unreinforced (pure) phenolic resin presented in Figure 3. Various oxygen arrangements in the structure of this resin including the vibration mode of epoxide (C-O-C) at 1235 cm^{-1} , ester (C=O) at 1600 cm^{-1} , carboxyl (COOH) at 1729 cm^{-1} , and hydroxyl vibrations at 3385 and 1051 cm^{-1} [19, 20]

are observed. Oxygen-containing groups provide suitable bases for chemical bonding between CNTs and the polymer. FCNTs which are holding higher oxygen groups offer better situation for chemical bonding between the CNTs and polymer matrix.

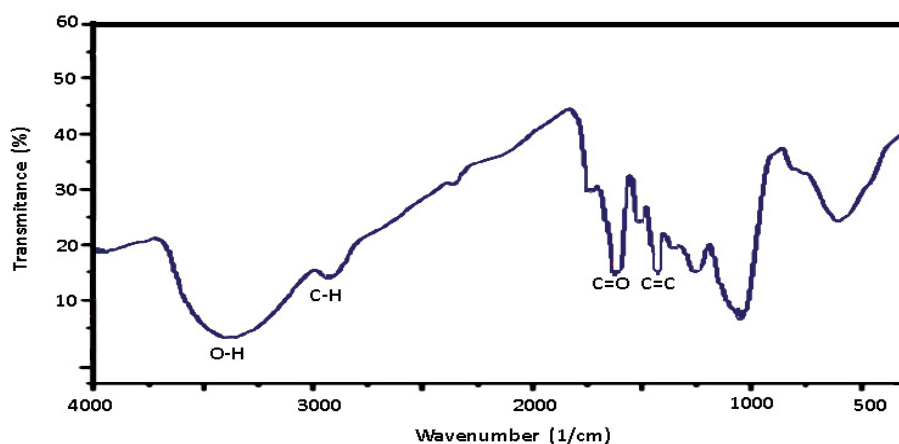


Figure 3. FTIR spectra of unreinforced phenolic resin which is used as a matrix of the nanocomposite.

Figure 4 shows the result of FTIR analysis of the composites containing carbon nanotubes; chemical functionalized or raw, and phenolic resin both after 2 hours milling. Although the addition of CNTs to the polymer matrix and also mechanical milling have caused some changes in the spectrum of the resin, FCNTs and raw CNTs are demonstrating a similar spectrum. Few small differences are observed between spectra of FCNTs/phenolic and raw CNTs/

phenolic including higher absorption of FCNTs/phenolic at 3400 and 1093 cm^{-1} wavenumbers (corresponding to O-H bonds) and also at 2923 cm^{-1} (corresponding to C-H bonds) and higher absorption of raw CNTs/phenolic at 1639 cm^{-1} (corresponding to C=C bonds). These results show that more oxidation has happened in the case of FCNT/phenolic composite, therefore more oxygen-containing groups are present in this nano-composite.

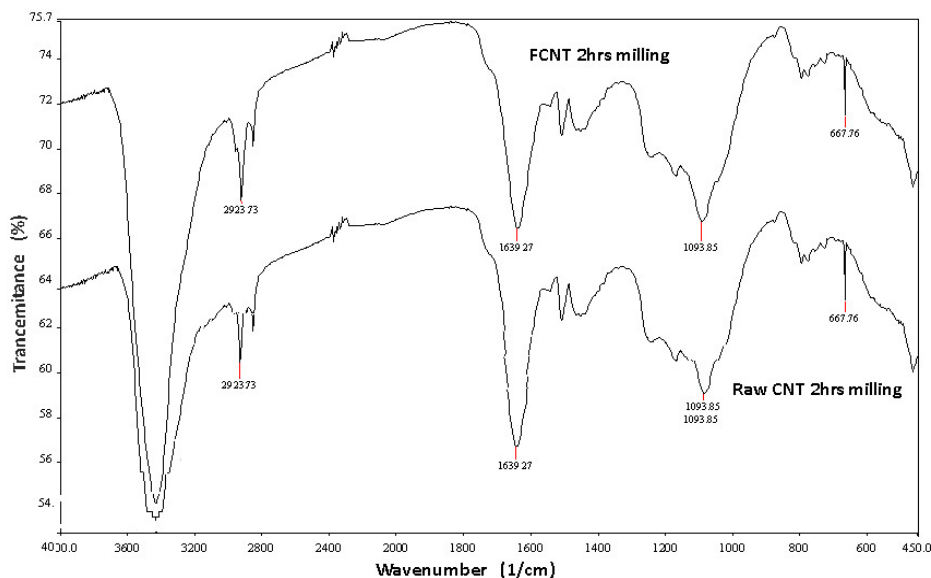


Figure 4. FTIR spectra of FCNTs/phenolic and raw CNT/phenolic composites after 2 hours milling.

FTIR spectrum of FCNTs/phenolic after 2 and 6 hours milling is presented in the Figure 5. Both composite show almost the same spectra, it appears that continuing ball milling of the composite more

than 2 hours has no noticeable effect on the chemical structure of the composite. The same result has been obtained for raw CNTs/phenolic composite.

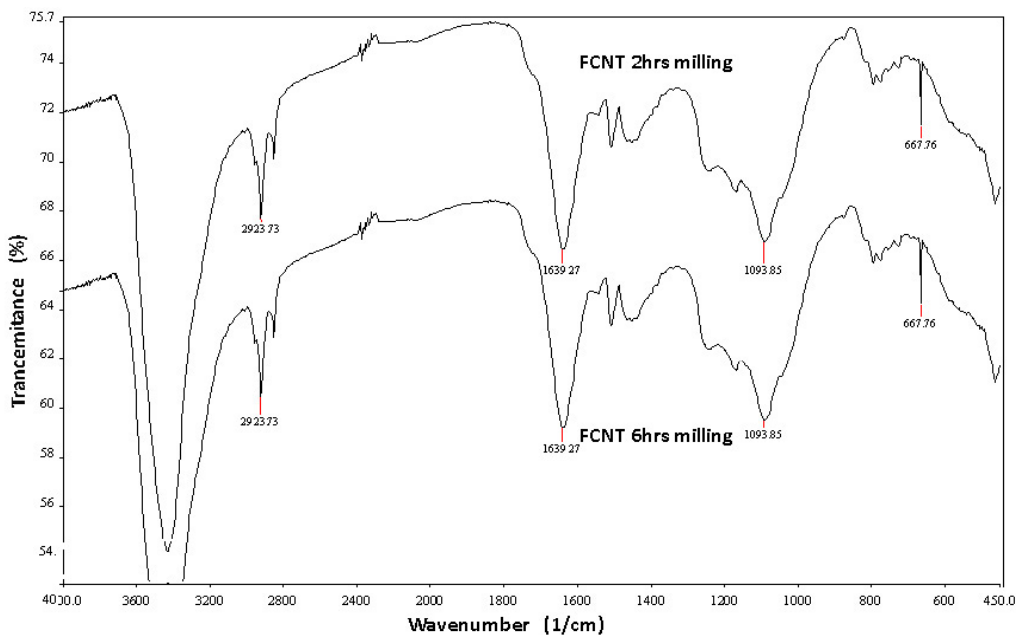


Figure 5. FTIR spectra of FCNTs/phenolic composite after 2 and 6 hours milling.

Figure 6 shows XRD pattern of carbon nanotubes under three different conditions; raw CNTs, FCNTs (0 hours milling) and FCNTs after 2 hours milling together with phenolic powder, all tested specimens exhibited a similar pattern including (002), (100), (004) and (110) planes of the CNTs. Increased intensity of (002)

peak in the FCNT pattern due to the purification of the CNTs during chemical functionalization and peak broadening in the case of FCNT 2 hrs milling due to mechanical functionalization are major differences between XRD pattern of the specimens.

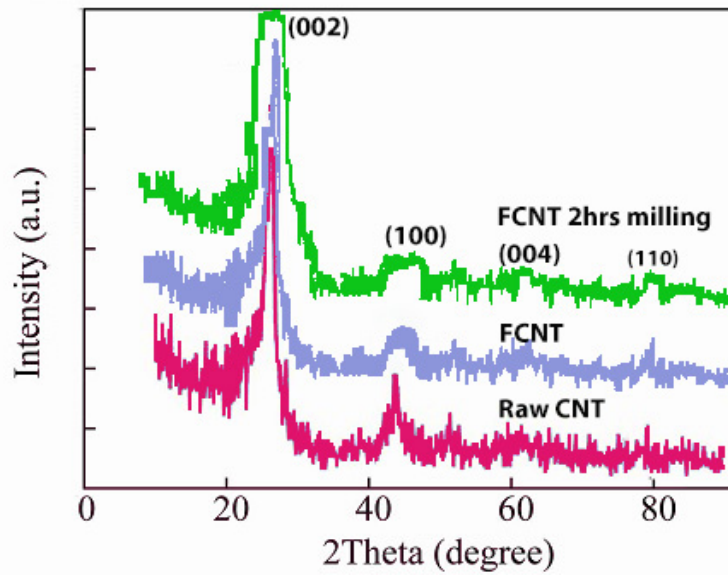


Figure 6. XRD pattern of carbon nanotubes under three conditions; raw CNTs, FCNTs 0 hours milling, and FCNTs after 2 hours milling.

TG curve of the composites and the unreinforced polymer is displayed in Figure 7. This graph shows three distinct areas in the behavior of the tested specimens, in the primary area which is between room temperature to 450 C° specimens lose less than 10 % of their weight and all of them exhibit same behavior in losing weight, this action is assigned to losing water, in the second area which is between 450 C° and 680 C° the specimens lose weight with a similar trend, in this area FCNTs/phenolic with 2 hours milling shows more residual weight and smaller slope in the weight loss, at the same condition FCNT/phenolic with 6 hours milling and unreinforced polymer shows less residual weight and greater slope in the weight loss this action is related to decomposition of the polymer.

In the tertiary area from 680 C° up to 800 C° while the composite specimens continuing their behavior from the previous area, unreinforced polymer shows higher residual weight and lower slope of weight loss this behavior is due to decomposition of the polymer and oxidation of the CNTs. Since the unreinforced polymer is free of the CNTs it is losing weight only by polymer decomposition, therefore, it loses less weight compared to composite materials. It may be concluded that among the composites FCNTs/phenolic with 2 hours milling shows more stable behavior and FCNT/phenolic with 6 hours milling performs less stability, the stability of FCNT/phenolic with 1 hours milling is between those two specimens.

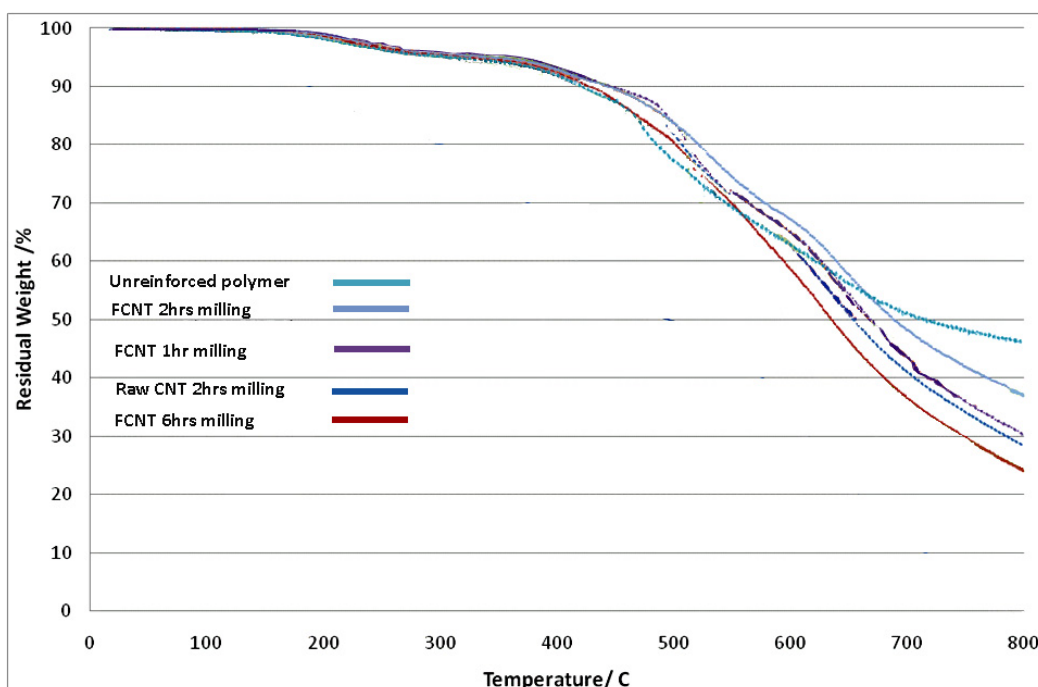


Figure 7. TG curve of the composites and unreinforced specimens.

Figure 8 shows the flexural strength of the FCNTs/phenolic and raw CNTs/phenolic composites. These results show that strength of the specimens which are made from chemical functionalized CNTs are higher than the strength of the composites made from raw CNTs regardless of the milling time. This behavior may

be attributed to improvement in CNT/matrix interface of the composites by chemical functionalization. On the other hand, both groups of the composites show an increase in strength with increasing milling time up to 2 hours, a small decrease in strength is observed with further milling.

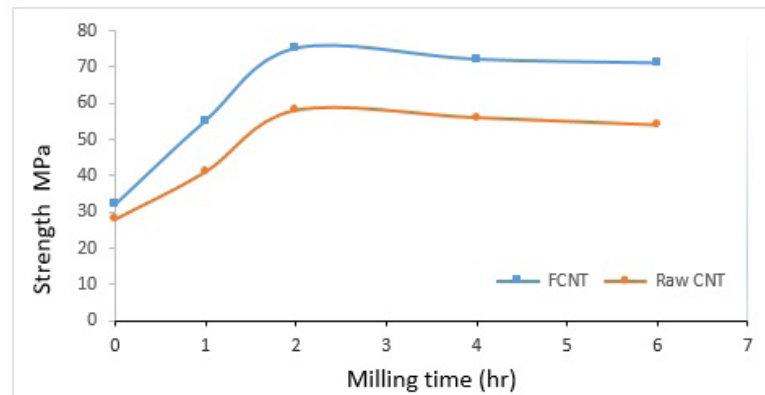


Figure 8. The flexural strength of the FCNTs/phenolic and raw CNTs/phenolic composites as a function of milling time.

Dissection

For the raw CNTs with a low concentration of oxygen-containing groups is difficult to react properly with the polymer matrix and produce strong CNT/matrix interface. During loading the material weak interfaces lead to create microvoids and crack at the CNT/matrix interfaces and reduces load carrying capacity and strength of the composite [21, 22]. Chemical functionalization changes the chemical structure of the surface of the CNTs and improves CNT/matrix interface by facilitation chemical reaction between CNTs and polymer matrix. The result of the thermogravimetric test shows higher residual weight of FCNT 2 hours milling composites compare to raw CNT 2 hours milling composites and provides further evidence for improving bonding of CNTs to the polymer matrix

On the other hand, due to high surface areas CNTs tend to create clusters, these clustering affects the mechanical property of the composites [8] another role of chemical functionalization is assisting better dispersion of the CNTs into the matrix [2].

The higher strength of a composite is obtained by a homogeneous distribution of a reinforcement into a matrix [2,5], mechanical functionalization through ball milling enhance distribution of the CNTs into the polymer matrix and increases contact between CNTs and polymer matrix lead to rising chemical bonding between them. Increase in milling period up to certain time improves mixing of the CNTs with the matrix, in the same time milling treatment, introduces damages into the CNTs and breaks them into the smaller parts. Increasing milling time increases damages and decreases aspect ratio of the CNTs and causes decrease in the strength of the composite [14]. A decrease in the crystallite size of CNTs by milling leads to peak broadening in XRD analysis which is observing in figure 6, in addition, damaged and broken CNTs tend to faster and easier oxidation and show lower stability in the

thermogravimetric test. Figure 7 shows lower residual weight for FCNT/phenolic 6 hours milling than FCNT/phenolic 2 hours milling. Results show that in the first stage, mechanical treatment improves CNTs/matrix interfaces and CNTs distribution as a result strength of the composite increases, in contrast, effect of long milling time (more than 2 hours) on the CNTs/matrix interfaces and CNT distribution is small, but its effect on damages and reducing aspect ratio of the CNTs is high and causes decrease in the strength of the composite.

Conclusions

Acid chemical functionalization introduces chemical changes into the surface structure of the CNTs and increases the concentration of the oxygen-containing groups. These chemical changes improve CNTs/matrix interface and raise the composite's strength.

Mechanical functionalization by ball milling improves CNTs distribution into the matrix and presents some changes in the surface structure of the CNTs and modifies the strength of the composite.

Mechanical milling creates damages on the CNTs and reduces the aspect ratio of the CNTs, therefore prolonging milling time decrease strength of the composite.

In the tested composite highest strength is obtained by chemical functionalization followed by 2 hours mechanical milling.

References

- [1] M. Tarfaoui, K. Lafdi, A. El Moumen, Mechanical properties of carbon nanotubes based polymer composites, *Composites Part B* 103 (2016) 113-121
- [2] T. Thostenson, Zuoguang Zhang, Joon-Hyung Byun, An assessment of the science and technology of carbon nanotube-based fibers and composites, *Composites Science and Technology* 70 (2010) 1-19

- [3] Yeh MK, Tai N-H, Liu J-H. Mechanical behavior of phenolic-based composites reinforced with multi-walled carbon nanotubes. *Carbon* 44 (2006), 1–9
- [4] R. Taheriana, M. J. Hadianfard, A. Nozad Golikandc, Manufacture of a polymer-based carbon nanocomposite as bipolar plate of proton exchange membrane fuel cells, *Materials & Design*, Volume 49 (2013), 242–251
- [5] S. Kumar Swain, Itishree Jean, Polymer/Carbon Nanotube Nanocomposites: A Novel Material, *Asian Journal of Chemistry*, 22, No. 1, (2010), 1-15
- [6] C. N. R. Rao, Achim Müller, Anthony K. Cheetham, *The chemistry of nanomaterials: synthesis, properties and application*, Wiley-VCH; (2004), 208-239
- [7] C.A. Dyke, M.J. Tour, Overcoming the insolubility of carbon nanotubes through high degrees of sidewall functionalization *Chemistry - A European Journal*, 10(4), (2004), 812-817
- [8] Sung-Hwan Jang, S. Kawashima, H. Yin, Influence of carbon nanotube clustering on mechanical and electrical properties of cement pastes, *Materials (Basel)*, 9(4), (2016), 220-236
- [9] M.E. Lipin´ ska, S.L.H. Rebelo, M.F.R. Pereira b, J.A.N.F. Gomes, C. Freire, J.L. Figueiredo, New insights into the functionalization of multi-walled carbon nanotubes with aniline derivatives, *Carbon*, 50 (2012) 3280 –3204
- [10] O-K. Park, H-S Chae, G. Y. Park, N-H You, S. Lee, Y. H. Bang, D. Hui, B-C Ku, J. H. Lee, Effects of functional group of carbon nanotubes on mechanical properties of carbon fibers, *Composites Part B* 76 (2015) 159-166
- [11] J. Amiran, V. Nicolosi, SD Bergin, U Khan, PE Lyons, JN Coleman, High quality dispersions of functionalized single walled nanotubes at high concentration. *J. Phys. Chem C*, 112(10), (2008), 3519–3524.
- [12] O-K Park, S Lee, H-I Joh, J K Kim, P-H Kang, J H Lee, B-C Ku, Effect of functional groups of carbon nanotubes on the cyclization mechanism of polyacrylonitrile (PAN), *Polymer* 53, (2012), 2168-2174
- [13] M. Moniruzzaman, J. Chattopadhyay, W. Edward Billups, K.I. Winey, Tuning the Mechanical Properties of SWNT/Nylon 6, 10 Composites with Flexible Spacers at the Interface, *Nano Lett.* 7(5), (2007), 1178-1185
- [14] D. Molina, *Polymer nanocomposites based on carbon nanotubes*, thesis, Politecnico di Milano, (2012)
- [15] B. Ribeiro¹, E. C. Botelho, M. L. Costa¹, C. F. Bandeira, Carbon nanotube buckypaper reinforced polymer composites: a review, *Polímeros*, 27(3), (2017), 247-255,
- [16] D. S. Ahmeda, A. J. Haider, M. R. Mohammad, Comparison of Functionalization of multi walled carbon nanotubes treated by oil olive and nitric acid, *Energy Procedia*, 36, (2013), 1111–1118
- [17] M. Vesali Naseh, A. A. Khodadadi, Y. Mortazavi, O. Alizadeh Sahraei, F. Pourfayaz, S. Mosadegh Sedghi, Functionalization of carbon nanotubes using nitric acid oxidation and DBD plasma, *World Academy of Science, Engineering and Technology*, 27, (2009), 567-569
- [18] Sudesh, N Kumar, S Das, C Bernhard, G D Varma, Effect of graphene oxide doping on superconducting properties of bulk MgB₂, *Supercond. Sci. Technol.* 26 (2013) 095008, 1-8
- [19] N. A. Abd Ghani, N. Izzati Zakaria, D. Samsudin, N. M. Abdul Wahab, N. Aishatun Majid, R. Daik and M. A. Mohd Ishak, New method for novolac type liquefied coconut coir Husk Lignin/ Phenol/ Formaldehyde resin, *Journal of Applied Science and Agriculture*, 10(5) Special (2015), 47-51
- [20] A. Bobrowski, B. Grabowska, FTIR method in studies of the resol-type phenol resin structure in the air atmosphere over certain time intervals, *Metallurgy and Foundry Engineering*, 41 (3), (2015), 107–113
- [21] M.J. Hadianfard, J. Healy and Y-W. Mai, Fracture Characteristics of a Particulate reinforced Metal Matrix Composite, *J. Mat. Sci.* 29 (1994), 2321-2327
- [22] K. Alasvand Zarasvand, H. Golestanian, Effects of Nanotube/Matrix Interface on Multi-Walled Carbon Nanotube Reinforced Polymer Mechanical Properties, *Mechanics of Advanced Composite Structures*, 4, (2017), 211-223

The Wear Behavior of Au-Co/Diamond-Like Carbon Composite Electrochemical Coating

S.M.M. Hadavi^{1*}, P. Gegan²

¹Tarbiat Modares University, Department of Materials Engineering, Tehran, I.R.Iran

²Azad University, Tehran Branch, Tehran, I.R.Iran

* Corresponding Author: s.hadavi@modares.ac.ir

Abstract

Gold—cobalt/nanodiamond composite coatings were deposited on a commercially pure copper substrate by electrodeposition method. Gold and cobalt salts of $\text{KAu}(\text{CN})_2$ and CoSO_4 were used as the coating electrolyte to have about 8 μm thick Au-0.6wt% Co coating layer. Nanodiamond particles of 5 nm in size were used in the electrolytes carrying 0, 5 and 12 g/l of these particles. By passing direct current for about 10 minutes, a composite coating including nanodiamond particles in the gold-cobalt matrix was formed. In order to reduce the amount of agglomeration of nano-particles, the electrolyte was agitated with ultrasonic waves of 20 kHz for about 20 minutes prior to the coating. The agitation of the electrodeposition bath was continued during coating treatment using mechanical stirrer. This caused the formation of relatively uniform distribution of nanodiamonds in the coating matrix. The effect of concentration of diamond nanoparticles in the plating solution on the micro hardness and wear resistance were studied. Wear resistance of the composite coatings was determined by “ball on disk” wear test where the weight loss of samples was reported as wear behavior. Results showed that the gold-cobalt nano-diamond composites possessed higher hardness and more wear resistance compared with those of gold-cobalt coating. Addition of 12 g/l nanodiamond to the electrolyte increases the coating micro harness and wear resistance to about 130 and 400 percent, respectively. These remarkable improvements in the wear properties of the gold-cobalt coatings are believed to be potentially useful in various applications in electronic industries as well as decorative applications.

Keywords: Diamond-Like Carbon (DLC); Gold Coating; Electro-deposition; Wear.

Introduction

In electronic industry the high electrical conductivity is required for high efficient contacts. On the other hand, gold in its pure state possesses high electrical conductivity. However, the corrosion resistance of gold is high enough such that in almost all working conditions is inert. This results in gold surface to be free from oxides and sulfides and therefore, its conductivity remains unaffected during service. These properties lead the designers to use gold coating on copper or other metals. In electronic industries gold coating is used in the connection points, semiconductor and microelectronics field, sealed reed relay contacts and general electrical connectors as it improves the conductivity [1]. But

gold coating possesses a weakness in its wear resistant. Electrical contacts need to be highly wear resistant in a way that plugging and unplugging do not remove the gold coating and hence, interfering the electrical conductivity.

Several efforts have been focused on improving the wear resistance of gold coating. Introducing nickel intermediate layer between the top gold layer and the substrate is a way to increase the corrosion as well as wear resistance of the coating. In fact, nickel layer provides a relatively high mechanical backing for the gold top layer.

It is logic to use a composite of gold coating with hard materials such as diamond particles. Diamond is known for its high hardness of about 6000 to 10000 HV [2]. That is the reason for synthetic production of diamond particle in large scale. In the study carried by Dub et al., [3] type-Ib synthetic diamond single crystals were synthesized by the spontaneous crystallization at pressures of 5.5–5.8 GPa and at temperatures of 1400–1420 °C. They reported the hardness of these particles to be about 80 GPa.

In this study nano-size particles of Diamond-Like Carbon (DLC) are incorporated in to gold-cobalt electroplating coating in order to increase its wear resistance.

Materials and experimental procedure

Gold-cobalt coating was performed using an acidic electrolyte in an electrochemical deposition system. Anode was selected from 316 stainless steel whereas cathode was commercially pure copper. Diamond like carbon with the size of about 5 nm was added to the electrolyte with the amounts of 5 and 12 mg/l. The used electrolyte and electrochemical coating parameters are mentioned in Table 1.

In order to prevent agglomeration of DLC particles in electrolyte, the coating bath was stirred with ultrasonic wave with 20 KHz frequency, for about 20 minutes prior to the coating process. During electrodeposition coating, the bath was stirred with mechanical stirrer. The speed of stirrer is important since low speed results in agglomeration and high speed leads to low efficiency of the coating process. The best speed was experimentally found to be about 100 rpm.

The current density is also very important. Low current density reduces the deposition of DLC in the coating, whereas high current density imparts contamination to the coating layer results in reducing its shiny surface and electrical conductivity [4].

Acidity (pH)	4-5
Current Density	1 A/dm ²
Temperature (°C)	37 ± 2
Deposition time (min)	10
Electrolyte composition	Tripotassium Citrate Citric acid Gold salt (KAu(CN) ₂): 6 g/l Cobalt salt (CoSO ₄): 1 g/l
DLC (g/l in electrolyte)	0, 5 and 12

Table 1. Coating parameters used in this study.

The micro hardness of the obtained coatings was measured with diamond pyramid indenter, 10 g force for 15 seconds.

The erosion behavior of the coatings was tested with ball on disc method. The sample discs were in 100 mm diameter and 5 mm thickness. The eroding ball was alumina with 1200 HV hardness. The loading force was fixed about 250 g. Figure 1 shows the wear testing instrument. The rotating speed of the disc was about 0.05 m/s and the tests were stopped after 1200 seconds, i.e., after 60 meter of wear.

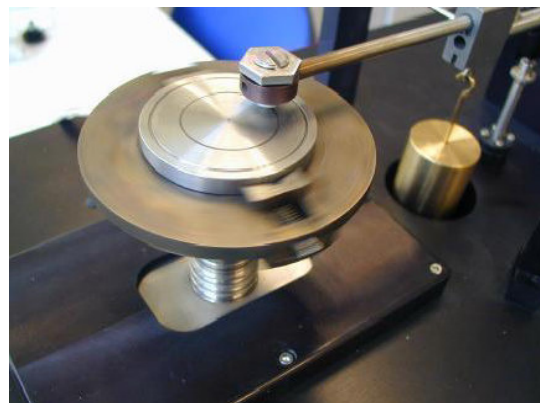


Figure 1. The instrument used for wear tests.

The topography as well as cross-sectional studies were performed by scanning electron microscopy VEGA-Tescan. The composition of the coatings was analyzed with the EDS system which was equipped with SEM.

Results and Discussions

Figure 2 shows the uniform equi-axed topography of the Au-Co coating. The cobalt content was measured to be about 0.6 wt%. The carbon content was less than the detection limit of EDS system.

Figure 3 shows the back-scatter image from cross-section of the Au-0.6wt%Co coating on copper substrate. Since atomic number of Au is much higher than that of copper, in back-scatter image Au coating is shown as brighter section. The coating was uniform with about 8 μm in thickness.

Figure 4 shows the surface topography of the Au-Co coating containing about 5 g/l DLC in the coating bath. It is clear that the structure differs from that of the coating without DLC. The EDS analysis revealed the presence of about 0.5-0.6wt%Co and about 12 to 14wt%C. It is clear that carbon represents nano-diamond particles in the coating.

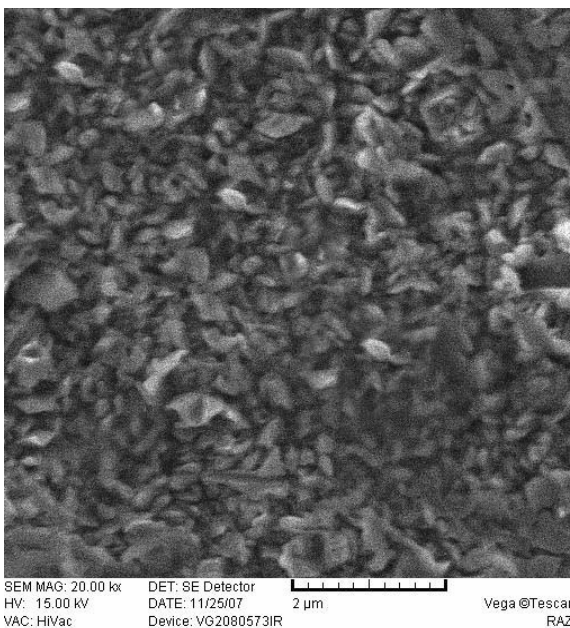


Figure 2. The SEM image of the Au-0.6wt% Co coating on copper.

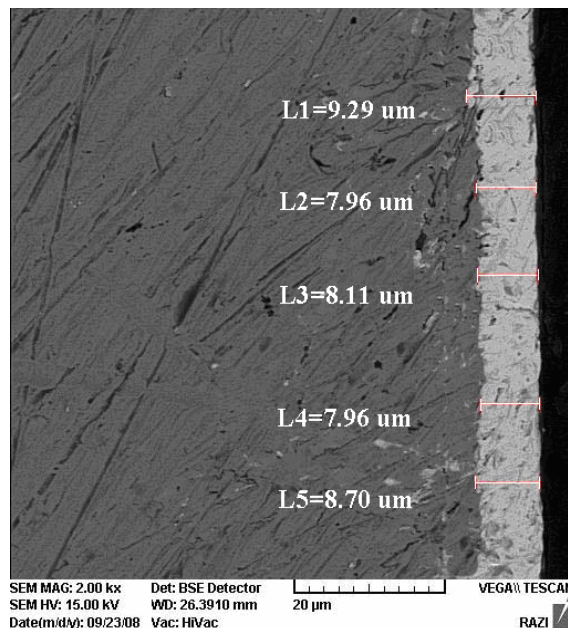
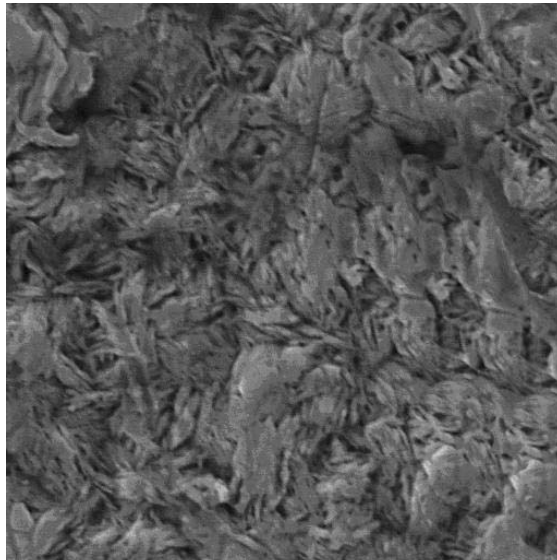
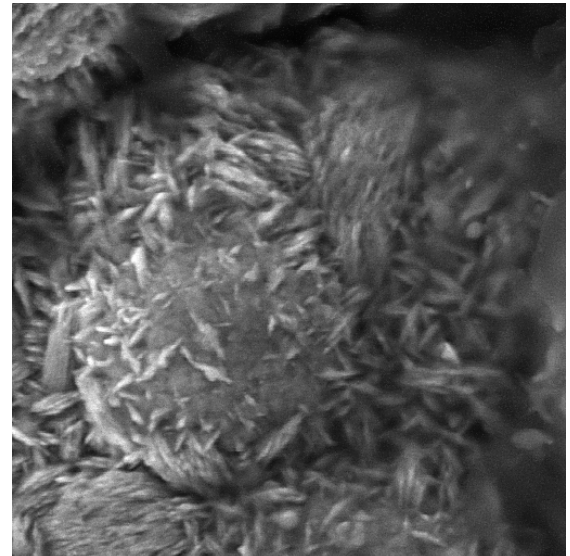


Figure 3. The SEM back-scatter image of the Au-Co coating on Copper substrate



SEM MAG: 8.00 kx HV: 15.00 kV VAC: HiVac DET: SE Detector DATE: 11/25/07 Device: VG2080573IR Vega@Tescan RAZI



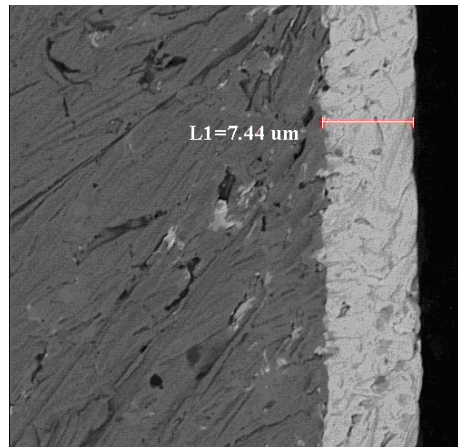
SEM MAG: 20.00 kx HV: 15.00 kV VAC: HiVac DET: SE Detector DATE: 10/01/07 Device: VG2080573IR Vega@Tescan RAZI

Figure 4. The surface structure of the Au-Co coating including 5% DLC in the coating bath.

Figure 5 shows the cross-section of the Au-Co coating which was applied while the electrolyte contained DLC of about 5 g/l. The figure shows a uniform coating layer of about 8 micrometer thickness.

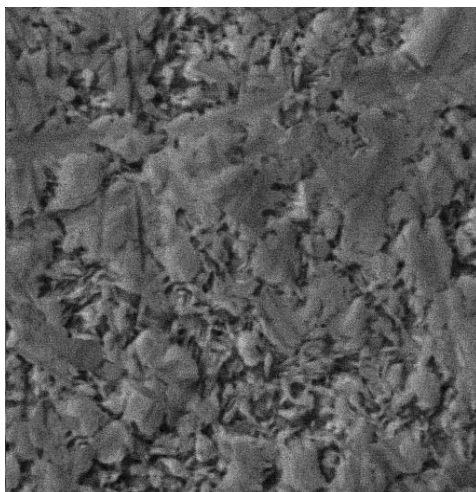
Increasing the amount of nano-diamond particles in the coating bath, increased the DLC content of the

coating, as detected by EDS system. Figure 6 shows the surface as well as cross-section of the Au-Co coating having 12g/l DLC in the coating bath. EDS analysis detected 0.55-0.65 wt%Co and 20-21wt%C in the coating.

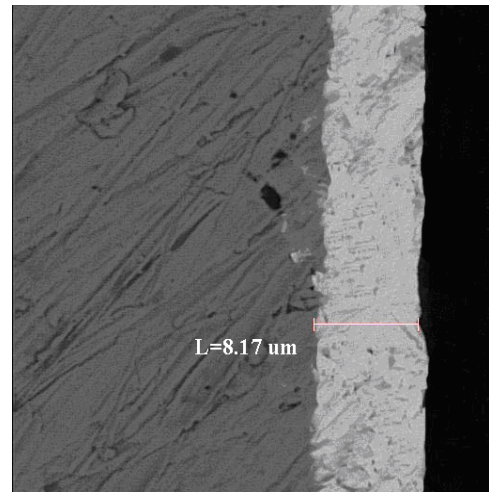


SEM MAG: 4.00 kx SEM HV: 15.00 kV Date(m/d/y): 09/23/08 Det: BSE Detector WD: 26.3530 mm Vac: HiVac VEGA@TESCAN RAZI

Figure 5. The SEM cross-section image of Au-Co coating containing 5g/l nanodiamond in the coating electrolyte.



SEM MAG: 15.00 kx SEM HV: 15.00 kV Date(m/d/y): 09/23/08 Det: SE Detector WD: 22.9920 mm Vac: HiVac VEGA@TESCAN RAZI



SEM MAG: 4.00 kx SEM HV: 15.00 kV Date(m/d/y): 09/23/08 Det: BSE Detector WD: 26.4150 mm Vac: HiVac VEGA@TESCAN RAZI

Figure 6. Surface as well as cross-section of the electrochemical Au-Co coating containing 12 g/l DLC in the coating bath.

Presence of diamond-like carbon in the coating increased the micro hardness of the coating layer. As figure 7 shows, the hardness of the Au-Co coating was about 135 HV, whereas addition of 5 and 12 g/l DLC to the coating bath increased the hardness to about 152 and 178 HV, respectively. The presence of DLC in the coating in the form of particles in metal matrix composite, increases the hardness due to the high hardness of the particles. It is reported, however, that increase in DLC content in the coating bath do not necessarily increase the coating hardness, as it may reduce the integrity of the coating matrix and lowers the coating adhesion to the substrate [5].

Surface analysis of the samples after wear, showed that the gold coating layer in the sample without DLC was removed by alumina ball while with the other two samples, a very thin layer was still remained. Figure 8 shows the sample surface of Au-Co/DLC (12g/l) composite coating after wear test. The line scan elemental analysis shows that although gold is to a large extent removed, the nano-diamond particles still remained on the surface and imparted an anchor role to keep the coating in place.

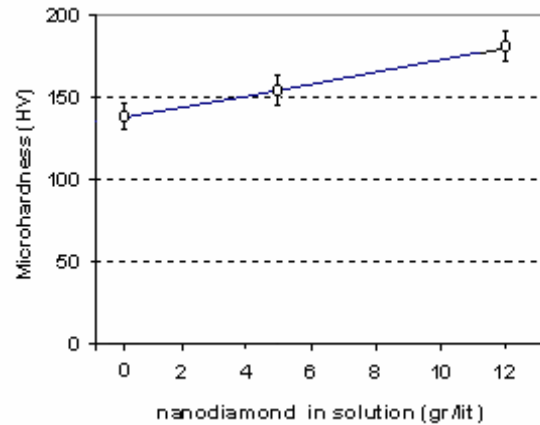


Figure 7. The micro-hardness measurement of the Au-Co electrochemical coating containing 0, 5 and 12 g/l in the coating bath.

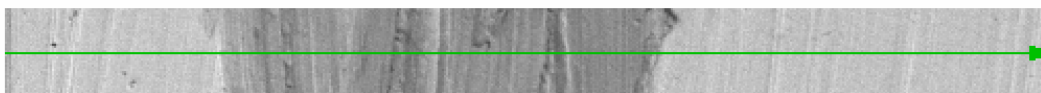
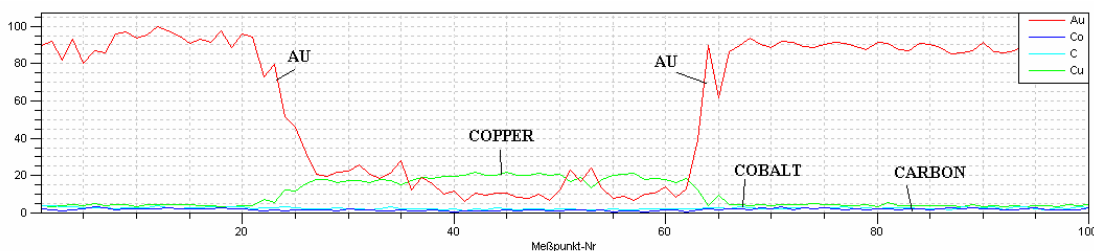
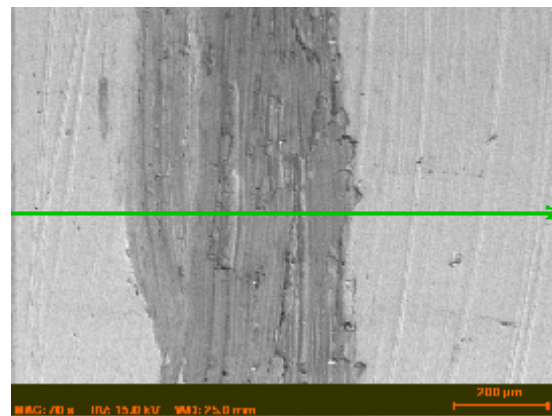


Figure 8. The SEM image of the sample surface with Au-Co/DLC (12g/l) composite coating after 60 m wear test. The line scan elemental analysis is also shown.

The elemental analysis of the wear section of the sample is presented in Fig. 9. It is evident that carbon and gold elements are still remained on the surface.

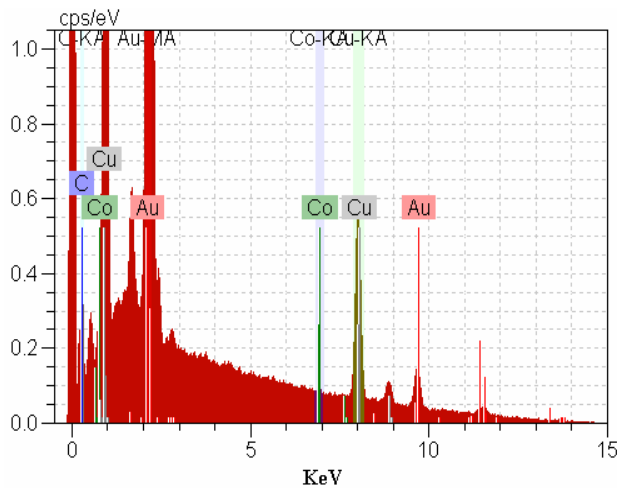


Figure 9. The elemental analysis of the wear section of sample shown in Fig. 8.

As the rotating speed, load and duration of the wear tests were fixed in all experiments, the weight reduction was considered as the symbol of wear behavior of the coatings. Figure 10 compares the weight loss of the samples after 60 m wear test. It is clear that the nano-particles imparted a notable wear resistance to the coating layer. In fact, presence of 5g/l nano-diamond in the coating bath resulted in improvement of the Au-Co wear resistance to about 150%. This improvement is more significant while 12 g/l DLC was included in the coating electrolyte, as it increased the wear resistance to more than 400%.

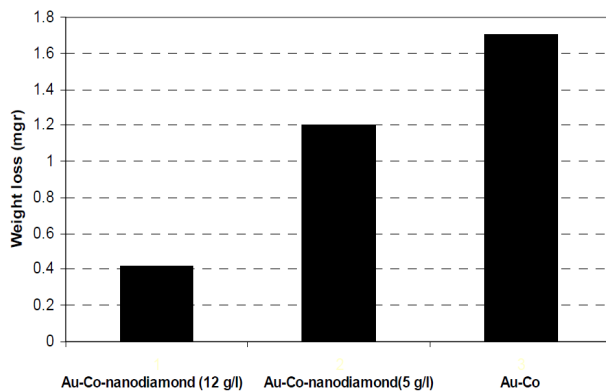


Figure 10. Weight loss of the samples after 60 m wear test.

The friction coefficients of the samples were recorded and the mean results are presented in Fig. 11. As it is shown the friction coefficient of the Au-Co coating reduced to its half by addition of 5g/l DLC to the coating bath. Interestingly, the friction coefficient was not significantly changed from 5 to 12 g/l DLC content in the coating electrolyte. This could be explained by wear mechanism which is mostly scratch rather than adhesion in coatings including DLC. In scratch mode, the hardness is more important than friction coefficient [6]. The cracks formed during wear test, as shown in Fig. 12a confirms the predomination of scratch mechanism in this study. However, for Au-Co

without DLC, no crack was detected on the eroded surface, showing a surface typical of adhesion mechanism for these coatings (Fig. 12b).

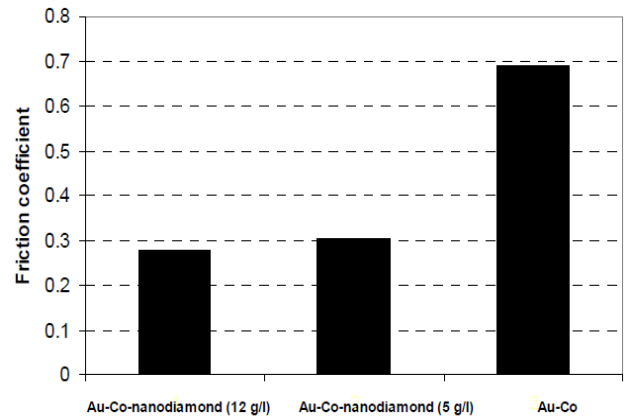


Figure 11. The mean friction coefficients of the Au-Co electrodeposition coating having 0, 5 and 12 g/l DLC in the coating bath.

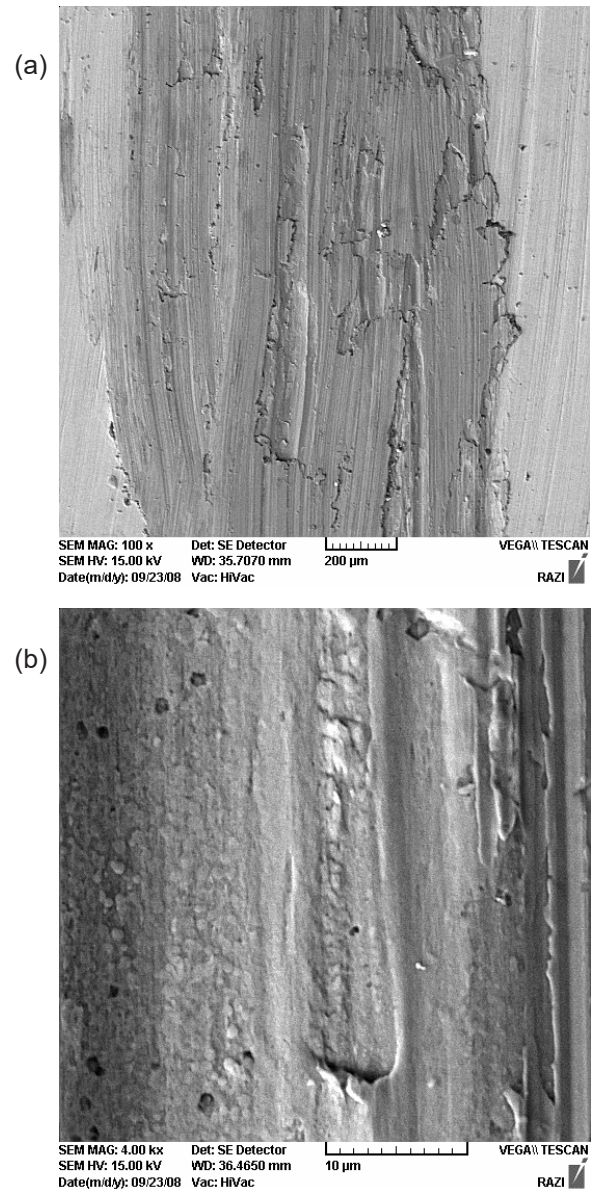


Figure 12. The eroded surface of (a) Au-Co/DLC (12g/l) and (b) Au-Co coating layers.

Conclusions

1. Addition of nan-sized diamond-like carbon to the Au-Co electrochemical bath resulted in incorporation of DLC in the coating layer.
2. The wear mechanism in Au-Co/DLC coatings were predominantly scratch whereas for the Au-Co coatings was adhesion.
3. The coating micro hardness increased significantly by imparting to the coating. The hardness increased to 150 and 400 percent by addition of 5 and 12 g/l to the coating bath, respectively.
4. Although the friction coefficient of the Au-Co coating layer was reduced considerably by addition of 5 g/l DLC to the coating electrolyte, further increase in DLC content did not change the coefficient as expected.

References

- ^[1] F. H. Reid, Gold Plating in the Electronics Industry, Gold Bulletin, (1973), Volume 6, Issue 3, pp 77–81.
- ^[2] K. Miyoshi, Structures and Mechanical Properties of Natural and Synthetic Diamonds, NASA/TM-107249, (1998).
- ^[3] S. Dub, P. Lytvyn, V. Strelchuk, A. Nikolenko, Y. Stubrov, I. Petrusha, T. Taniguchi, S. Ivakhnenko, Vickers Hardness of Diamond and cBN Single Crystals: AFM Approach, Crystals (2017), 7, 369, pp: 1-13.
- ^[4] E. Noloubnin, S.M. Pimenov, A. Blatter, F. Schwager and P. Y. Dektov, Electroplating of Gold-Nanodiamond composite coatings, New Diamond and Frontier Carbon Technology, (1999), vol. 9, pp. 273-282.
- ^[5] P. Cojocar, A. Vicenzo, P.L. Cavallotti, Electrodeposition of Au/nanosized diamond composite coatings, J Solid State Electrochem (2005) 9: 850–858.
- ^[6] J. Molinari, R. Aghababaei, T. Brink, L. Frerot, E. Milanese, Adhesive wear mechanisms uncovered by atomistic simulations, Friction, 6(3): 245–259 (2018).

Socios protectores del Grupo Español del carbón



Industrial Química del Nalón, S.A.
NalónChem



ELCOGAS